STRATEGIES FOR APPLYING ACTIVE SEISMIC SUBGLACIAL TILL CHARACTERIZATION METHODS TO VALLEY GLACIERS

By

Jenna M. Zechmann, B.A.

A Thesis Submitted in Partial Fulfillment of the

Requirements for the Degree of

Master of Science

in

Geophysics

University of Alaska Fairbanks

May 2017

APPROVED:

Martin Truffer, Committee Chair
Christopher F. Larsen, Committee Co-Chair
Bernard J. Coakley, Committee Member
Jason M. Amundson, Committee Member
Paul J. McCarthy, Chair,
Department of Geosciences
Paul W. Layer, Dean,
College of Natural Science and Mathematics
Michael A. Castellini, *Dean of the Graduate School*

Abstract

Subglacial materials play an important role in glacier dynamics. High pore-pressure, high porosity (dilatant) tills can contribute to high basal motion rates by deforming. Amplitude Variation with Angle (AVA) analysis of seismic reflection data uses the relationship between basal reflectivity and reflection incidence angle to characterize the subglacial material. This technique can distinguish between dilatant tills and less-porous, non-deforming (dewatered) tills due to their distinctive reflectivity curves. However, noise from crevasses and glacier geometry effects can complicate reflectivity calculations, which require a source amplitude derived from the bed reflection multiple. We use a forward model to produce synthetic seismic records, including datasets with and without visible bed reflection multiples. The synthetic data are used to test source amplitude inversion and crossing angle analysis, which are amplitude analysis techniques that do not require absolute reflectivity calculations. We find that these alternative methods can distinguish subglacial till types, as long as reflections from crevasses do not obscure the bed reflection. The forward model can be used as a planning tool for seismic surveys on glaciers, as it can predict AVA success or failure based on crevasse geometries from remote sensing data and glacier bed geometry from radar or from a worst-case-scenario assumption of glacier bed shape.

Applying lessons from the forward model, we perform AVA on a seismic dataset collected from Taku Glacier in Southeast Alaska in March 2016. Taku Glacier is a valley glacier thought to overlay thick sediment deposits. It has been the subject of numerous studies focusing on its ice-sediment interactions. Our analysis indicates that Taku Glacier overlies unconsolidated tills with porosity values greater than 33 %, though because of uncertainties due to the lack of a bed reflection multiple, it is possible that the tills are not dilatant.

Table of Contents

List of Figures

List of Tables

1 Introduction

1.1 Importance of subglacial till

Glacier bed processes influence glacier behavior. Glacier flow models that incorporate basal motion must account for these mechanisms. The hydraulic diffusivity, shear strength, granulometry, and quantity of subglacial sediments affect till shear strength and ice-till coupling and thus determine basal sliding and sediment deformation (*Iverson et al.*, 1998, 1994; *Tulaczyk*, 1999). These till properties also control the evolution of the subglacial drainage network (*Walder and Fowler*, 1994; *Hewitt*, 2011) and the timing and intensity of responses to water inputs (*Truffer et al.*, 2009). Sediment production and erosion allow tidewater glaciers to advance and retreat independently of climate (*Motyka and Begét*, 1996; *Post and Motyka*, 1995; *Alley*, 1991). Glaciers in turn impact subglacial sediment shear strength and porosity (*Iverson et al.*, 1998; *Alley et al.*, 1987; *Truffer et al.*, 2000, 2001).

Subglacial tills can be well-consolidated, or able to enter a deformation regime. Of the latter, high porosity ($>40\%$) tills usually have high pore-pressure and are soft and deformable (*Iverson et al.*, 1998; *Iverson*, 2010). They are referred to as 'dilatant', [1] while lower porosity ($\sim 30\%$) tills are stiffer, not considered to be deforming, and referred to as 'dewatered'. Dilatant tills can contribute to glacier motion by deforming at their top few centimeters or decimeters (*Tulaczyk*, 1999) (Figure 1) or by allowing easy passage of clasts stuck to the glacier sole (*Iverson et al.*, 1995).

In ice sheet settings, dilatant tills underlie areas of fast-sliding ice (ice streams), while dewatered tills exist under slow-moving ice (*Alley et al.*, 1987; *Anandakrishnan et al.*, 1998; *Peters et al.*, 2006, 2008; *Peters*, 2009; *Christianson et al.*, 2014). *Vaughan et al.* (2003) observed a positive correlation between basal slipperiness (the ratio of basal velocity to basal shear stress) and sediment porosity in surveys of Antarctic ice streams. *Christianson et al.* (2014) found that tills near the onset of the Northeast Greenland Ice Stream showed a transition from consolidated outside of the ice stream, to dewatered within the shear margin, to dilatant underneath the ice stream. *Luthra et al.* (2016) found localized dewatered tills underlaying a sticky spot in Whillans Ice Stream; surrounding tills were dilatant. Patches of dilatant and dewatered tills can exist together over small spatial scales (tens of meters) without surface expression (*Vaughan et al.*, 2003; *Booth et al.*, 2012; *Reinardy et al.*, 2011).

Plastic rheology models often explain till deformation behavior (*Iverson et al.*, 1998; *Rath-*

[1] Dilatant till is defined herein as 'simply [a till] that has expanded by enlarging pore spaces with water' (*Clark*, 2010).

bun et al., 2008). Additionally, till yield stress depends on effective pressure (*Kamb*, 1991). Thus till pore pressure increases reduce till yield strength and can activate viscous till deformation (*Hart et al.*, 2011). *Walter et al.* (2014) and *Hart et al.* (2011) suggest that tills can switch between dilatant and dewatered states over seasonal or yearly timescales due to subglacial water pressure changes. Sediment changes can also account for the activation and deactivation of ice streams (*Vaughan et al.*, 2003).

Whereas dilatant tills can deform, and dewatered tills can enter a deformation regime, well-consolidated tills cannot undergo viscous deformation under glacier shear stresses and basal motion may occur only via sliding or brittle till failure (*Truffer and Harrison*, 2006). We must know till dilatancy and consolidation to choose the correct basal boundary conditions when modeling glacier motion.

Tills also determine patterns of glacial erosion. The presence of a till layer slows bedrock erosion by at least one order of magnitude, or prevents erosion altogether if the till is not deforming at its base (*Cuffey and Alley*, 1996). Thus maps of subglacial till distribution are necessary for erosion studies.

In tidewater glacier settings, subglacial sediments have a dramatic impact on glacier evolution. Rates of till evacuation determine how quickly a tidewater glacier can advance (*Alley*,

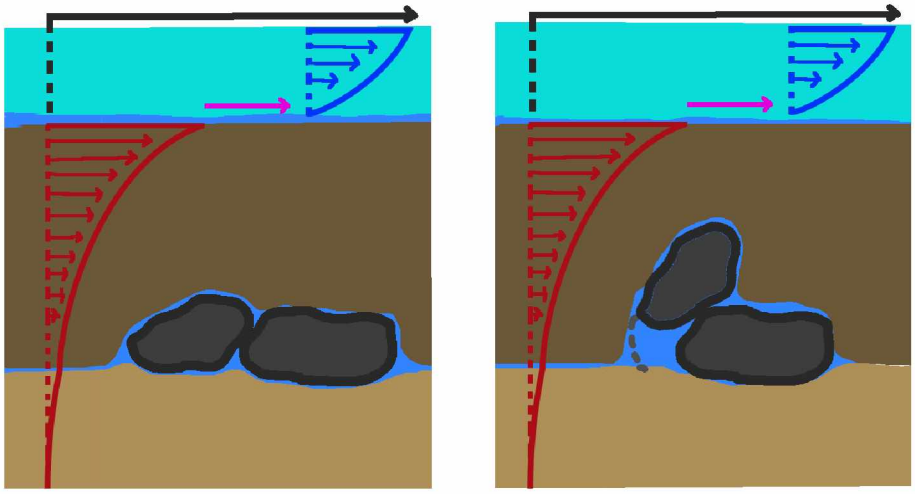

Figure 1: Mechanisms for glacier basal motion and till dilation. Glacier surface velocity (black arrows) is attributed to ice internal deformation (blue arrows) and can be augmented by sliding at the glacier sole (magenta arrows) and/or sediment deformation (red arrows). Till deformation can result in till dilation. Pore spaces are small prior to deformation (left panel) and enlarge as grains move past one another (right panel).

1991). Where a tidewater glacier has overridden soft tills, subglacial fluvial action is the greatest cause of erosion (*Motyka et al.*, 2006), and till properties affect the geometry of the subglacial fluvial system. Till deformation further increases erosion as it conveys tills to subglacial channels (*Walder and Fowler*, 1994).

Till type and location are difficult to predict from surface observations. We require specialized methods to observe subglacial tills and study ice/sediment interactions. The best way to study till is in-situ, because exposed tills lose their dilatancy and experience granulometry changes over timescales of less than a year (*Boulton and Dent*, 1974). In-situ till studies require borehole instrumentation or geophysical methods. Geophysical methods carry an advantage over borehole methods because they can observe large areas and are logistically easier to perform, and unlike sediment coring (*Talalay*, 2013), cannot alter till properties and skew results.

1.2 Seismic studies of subglacial till

Amplitude Variation with Angle (AVA) analysis of seismic data can reveal the density of a layer (ρ) and the velocities of seismic waves that travel through that layer (*Sheriff and Geldart*, 1995). It expresses sediment layer reflectivity against seismic wave incidence angle and inverts for α (compressional wave velocity), β (shear wave velocity), and ρ (density) using the Zoeppritz equations or approximations thereof (*Zoeppritz*, 1919; *Aki and Richards*, 2002; *Booth et al.*, 2016). These equations describe the relationship between seismic parameter contrasts across an interface (i.e., the glacier bed) and the reflectivity of that interface (see Figure 2).

AVA is performed on active seismic reflection data. In seismic reflection surveys, a line of receivers (geophones) along the ground records waves from an artificial, impulsive energy source (a 'shot') at the surface. Interfaces between two subsurface layers of contrasting seismic parameters (compressional wave velocity α, shear wave velocity β, and density ρ) will cause energy to be reflected back towards the receivers. Multiple receivers at a regular surface interval allow a range of incidence angles to be predicted and recorded. Multiple shot locations make it possible to sample many parts of the interface over a range of incidence angles and provide multiple independent reflections at each incidence angle which we may stack to increase the signal-to-noise ratio in the dataset.

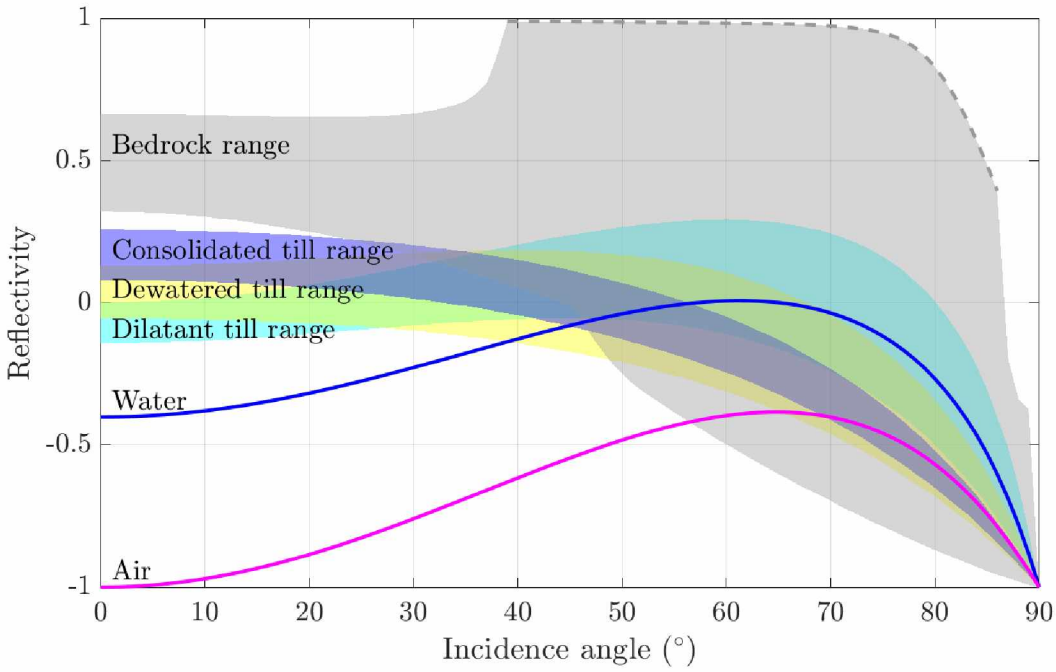

Figure 2: Reflectivity curves and curve ranges for interfaces between glacier ice and various materials. Seismic parameters used to produce these ranges are listed in Table 1. Water can be distinguished from other glacier bed materials by its negative polarity at all incidence angles. Bedrock can be distinguished from dewatered or lithified tills by its high reflectivity at near offsets, a sudden reflectivity increase at its critical angle, and a sudden switch to negative polarity at greater incidence angles.

Reflection amplitudes are determined from the seismograms produced by the survey, and reflectivities are calculated from these amplitudes. Reflectivity calculation requires a knowledge of the shot amplitude. Shot amplitude is not measured directly, but instead it is determined from comparing the amplitudes of the interface reflection and its multiple. The multiple wave is energy that has traveled to the interface and back to the surface twice. Layer reflectivities are plotted against incidence angle, and a best-fit curve is determined using the Zoeppritz Equations.

The AVA method has become an important tool in the fossil fuel industry, where it is used to distinguish rocks with oil- or gas-filled pores from rocks with brine-filled pores (*Castagna et al.*, 1998). AVA has also found application in glaciological studies. A till porosity change from 30% to 40% can have an obvious effect on the AVA curve (Figure 2). Even more obvious are the differences between tills, bedrock, and water interfaces such as subglacial lakes.

Table 1: Values used to produce the curves in Figure 2. Till values are from density measurements of till deposits (*Clarke et al.*, 2008), shear wave velocity measurements of marine sediments (*Hamilton*, 1976), density–compressional wave velocity relationships in marine sediments (*Morgan*, 1969), and an AVA study by *Christianson et al.* (2014).

Material	α ($\mathrm{m\,s^{-1}}$)	β ($\mathrm{m\,s^{-1}}$)	ρ ($\mathrm{kg\,m^{-3}}$)
Dilatant till	1500–1800	0–500	1700–2000
Dewatered till	1600–2000	400–1100	1900–2200
Consolidated till	1900–2300	1000–1200	2100–2500
Bedrock	3000-6000	1500-3000	2200-2800
Water	1450	0	1000
Air	340	0	1.2
Glacier ice	3700	1850	917

The AVA method can characterize materials by measuring their density and seismic wavespeeds. Seismic wavespeeds are elastic parameters which we can use to infer other sediment characteristics. The compressional wave velocity α reflects sediment consolidation and water content. Shear wave velocity β reflects sediment shear strength and pore pressure (*Hamilton*, 1976) and is even more sensitive to water content than α. ρ is inversely related to water content. α, β, and ρ of a medium are related to its material properties as follows:

$$\alpha = \sqrt{\frac{\lambda + 2\mu}{\rho}} \tag{1}$$

$$\beta = \sqrt{\frac{\mu}{\rho}} \tag{2}$$

λ is the Lame's first parameter (an elastic modulus) and μ is shear modulus, which is zero in a fluid (*Sheriff and Geldart*, 1995).

Calculated α, β, and ρ values allow us to categorize subglacial materials. Table 1 shows typical seismic velocity and density ranges for various materials found beneath glacier ice. Typical temperate glacier ice seismic parameters are also shown.

The dilatant till and dewatered till density ranges shown in Table 1 are derived from exposed till deposits (*Clarke et al.*, 2008). We assume that these exposed till deposits had average porosities of 30%, and derived a minimum dilatant till density by extrapolating to 50% porosity, with an upper limit at the minimum exposed till density. Minimum α values for

dewatered and dilatant tills are chosen using observed α-ρ relationships in marine sediments (*Morgan*, 1969). Shear wave velocities for various saturated marine sediments range from $\sim 50\,\mathrm{m\,s^{-1}}$ to $450\,\mathrm{m\,s^{-1}}$ (*Hamilton*, 1976), and we adopt the range $0\,\mathrm{m\,s^{-1}}$ to $500\,\mathrm{m\,s^{-1}}$ for dilatant tills. We assume dewatered tills range from $400\,\mathrm{m\,s^{-1}}$, to $1100\,\mathrm{m\,s^{-1}}$, the maximum β value found from AVA analysis of unconsolidated tills (*Peters et al.*, 2007).

α, β, and ρ ranges for a consolidated till are from *Christianson et al.* (2014). The water curve in Figure 2 is reproduced with $\beta = 0$ and $\alpha = 1450\,\mathrm{m\,s^{-1}}$ (*Medwin*, 1975).

Table 2 summarizes till velocity findings from past AVA experiments, with the authors' interpretations of till type. There is only one example of seismic velocities derived from travel time inversion (*Blankenship et al.*, 1987). *Blankenship et al.* (1987) were able to do this because they successfully recorded both compressional and shear wave reflections from the top and bottom of a subglacial sediment layer. Most glacier seismic surveys cannot rely on generating or recording shear-wave reflections, so β generally may only be found using AVA analysis.

In order to employ AVA analysis we require accurate amplitudes from the glacier bed reflection. The usual AVA workflow also requires us to obtain reliable amplitude measurements of the bed reflection multiple, to reconstruct the energy of the source wavelet. We must also eliminate all other sources of amplitude variation in the bed reflection before calculating reflectivity. This requires us to have accurate measurements of attenuation in the ice, seismic energy sources that transmit energy to the ice with well-reproduced amplitudes, and recording devices (geophones) that all couple with the glacier surface to the same high degree[2]. Also, we need an accurate model of the glacier bed shape to know the incidence angles ϕ of the bed reflections and the lengths of seismic rays. Glacier conditions can prevent us from satisfying these requirements. Complex glacier geometries produce uncertainties in ϕ. Surface waves (groundroll, a.k.a. Rayleigh waves) superimpose on the bed reflection and can obliterate parts of it, especially if the ice is thin. Bed reflections from thin glaciers can also suffer contamination from direct waves reflecting off of crevasses (Figure 3).

[2]We use the term 'shot-geophone coupling' to refer to variability in recorded amplitudes attributable to heterogeneities in the amount of energy that shots impart to the glacier ice and the seismic energy recording efficiency of each geophone.

Table 2: Subglacial sediment properties from seismic surveys

Study and Location	Methodology	α ($\mathrm{m\,s^{-1}}$)	β, ($\mathrm{m\,s^{-1}}$)	ρ,($\mathrm{kg\,m^{-3}}$)	Till type
Blankenship et al. (1986) Whillans Ice Stream	Reflection travel time inversion	1600 ± 100	150 ± 10	0.4 porosity	dilatant
Anandakrishnan (2003) Kamb Ice Stream	Crossing angle	~ 1700	100 ± 200	—	dilatant
Peters et al. (2006) Bindschadler Ice Stream	CMP velocity analysis	1580 ± 150	—	—	dilatant
Peters (2009) Kamb Ice Stream	AVA	1650–1750	300–400	1700–1900	dilatant
Peters et al. (2007) Bindschadler Ice Stream	AVA	1650 ± 150	200 ± 50	1750 ± 150	dilatant
		1800 ± 150	1000 ± 100	1900 ± 150	dewatered
Christianson et al. (2014) Northeast Greenland Ice Stream	AVA	1700 ± 250	250 ± 150	1800 ± 100	dilatant
		1700 ± 200	600 ± 200	1750 ± 300	dewatered
		2100 ± 200	1100 ± 100	2300 ± 200	consolidated
Luthra et al. (2016) Whillans Ice Stream Sticky Spot	AVA	1840 ± 180	310 ± 34	1835 ± 180	dewatered
Taku Glacier terminus; forward model	hypothesized	1700	200	1800	dilatant

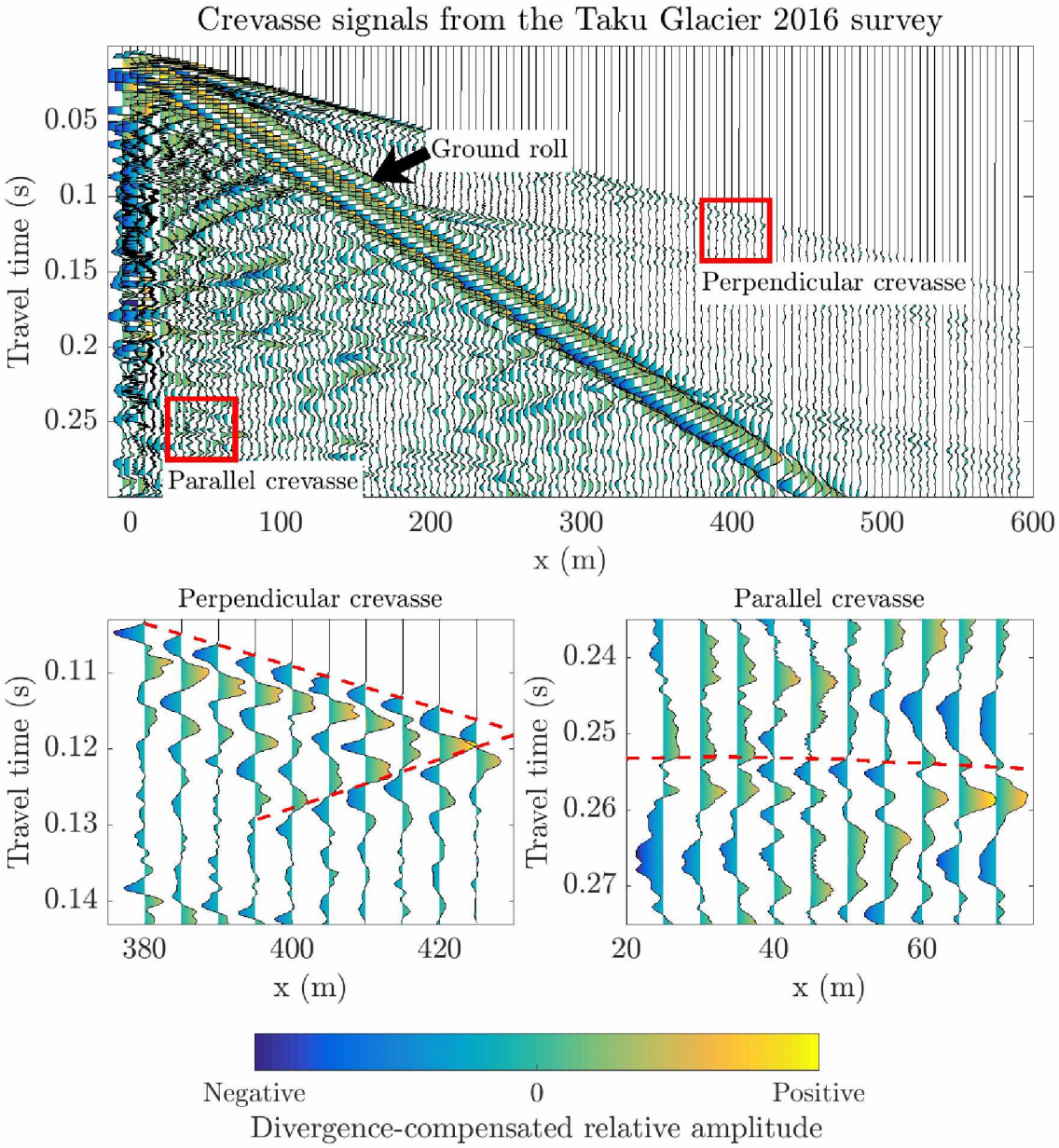

Figure 3: An example of a raw seismic record from a survey performed on Taku Glacier, a valley glacier with crevasses that ranged from perpendicular to parallel with the seismic line. Unwanted signals caused by these crevasses appear in the seismic gather. Crevasses perpendicular to the seismic line produce backscattered signals in the direct wave (see red dashed line in the lower left inset) and crevasses parallel to the seismic line appear as hyperbolic reflectors (lower right inset). The groundroll also experiences backscattering in a similar manner.

Ice sheets are good candidates for AVA surveys due to their thick ice, sparsity of crevasses, and surface-parallel bed geometries. Valley glaciers, however, often yield poor results. They can be thin, highly crevassed, and geometrically complex. For these reasons valley glaciers are generally not chosen as candidates for AVA surveys, even though studies of their basal material would be useful.

Some data processing methods exist that can aid analysis of these low-quality datasets. Trace stacking can increase signal-to-noise ratio (*Navarro et al.*, 2005; *Babcock and Bradford*, 2014). Bandpass filtering can also reduce groundroll noise, as long as the frequency ranges of the groundroll and compressional waves do not largely overlap. FK filters also can remove groundroll noise if geophones are spaced closely enough that groundroll is not spatially aliased. We can use seismic imaging and raytracing to estimate seismic reflection angles when geometries are complex. If after these efforts the bed reflection multiple is still obscured, reflectivity cannot be calculated.

The inability to calculate reflectivity does not always prevent the measurement of α, β, and ρ. We can adapt the AVA inversion method to use only relative bed reflection amplitudes. *Dow et al.* (2013) and *Anandakrishnan* (2003) have applied AVA principles to noisy datasets by adjusting the usual AVA workflow. *Dow et al.* (2013) worked with seismic data from Russell Glacier in West Greenland, which lacked a bed reflection multiple due to crevasse dispersion noise. They were still able to obtain a range of acceptable AVA curves by inverting for the source amplitude. *Anandakrishnan* (2003) analyzed sediments using a dataset with unreliable reflectivity values (due to the style of seismic acquisition, which used towed snow streamers instead of geophones) from the upper part of the Kamb Ice Stream, using the incidence angles of observed reflectivity reversals to constrain the AVA curve.

Other seismic studies have relied on only the polarity of the bed reflection to observe changes in basal conditions. *Richards* (1988) observed seismic phase reversals during the surge of Variegated Glacier, which he attributed to changes in basal sediments. This method cannot always distinguish saturated and dewatered sediments (see Figure 2). *Richards* (1988) also kept the seismic line as far from crevasses as possible to minimize groundroll noise.

To avoid problems from complex bed geometries, other scientists have taken advantage of local flat spots. *King et al.* (2008) performed reflectivity surveys at Midtre Lovenbreen, a small valley glacier in Svalbard. This survey used primary and multiple reflections from a surface-parallel planar part of the bed to determine a value for normal incidence reflectivity that was used to compare the strengths of bed arrivals elsewhere on the glacier, and revealed transitions between frozen talus and bedrock. *Babcock and Bradford* (2014) performed a seis-

mic reflection survey on Bench Glacier, another valley glacier, with a steep, undulating bed. Like *King et al.* (2008), they focused on obtaining data from a small flat area, and stacked multiple wavelets to increase signal-to-noise ratio for a full waveform inversion analysis of a thin basal ice layer.

Following *Dow et al.* (2013) and *Anandakrishnan* (2003), we will test the use of crossing angle analysis and source amplitude inversion on noisy seismic datasets, including modeled datasets and real data from Taku Glacier in Southeast Alaska. To start, we will discuss our seismic data from Taku Glacier, the characteristics of its reflections and confounding signals, and our hypothesis of the subglacial material type based on prior information. We then present a forward model for seismic wave propagation based on parameters derived from the Taku dataset. After that, we detail the data processing steps that we employ in AVA analysis. We describe the results from synthetic model runs and analysis of the Taku 2016 dataset, before moving on to a discussion of our results and conclusions that we draw from this study.

2 Taku Glacier surveys

Taku Glacier is a tidewater glacier in Southeast Alaska, currently in its advancing phase and protected from subaquous melt and calving by a proglacial shoal (Figure 4). It offers us a unique opportunity to study sediments under a tidewater glacier terminus, for it experiences low strain rates compared to other Alaskan tidewater glaciers (*Truffer et al.*, 2009; *O'Neel et al.*, 2003; *Pfeffer et al.*, 2000), resulting in a lower degree of crevassing which allows us to perform seismic reflection surveys on its surface. We performed such a survey in March of 2016 in order to obtain observations of Taku subglacial sediment qualities using Amplitude Versus Angle analysis. The seismic line was located in the ablation area, $\sim 1\,\mathrm{km}$ from the terminus, and oriented perpendicular to glacier flow (Figure 4).

2.1 Taku Glacier ice-sediment dynamics

Taku Glacier experiences tidewater advance and retreat cycles that have been asynchronous with climate fluctuations. Tidewater glacier advance and retreat is controlled by bedrock shape and sediment dynamics and modulated by climate (*Post*, 1975). Taku Glacier has undergone many cycles of advance and retreat in the past 3000 years (*Motyka and Begét*, 1996). The most recent retreat began in 1750 C.E. (*Post and Motyka*, 1995).

In its advancing phase Taku Glacier is stabilized by a proglacial shoal, which shields the ice from the mechanical stresses and heat transfer of Taku Inlet. During this phase the glacier advances by excavating subglacial sediments and expelling them in debris flows to form this shoal. As the glacier excavates sediments, its bed takes on a shape that deepens in the upglacier direction. Once sediment loss triggers a retreat, the glacier will rapidly lose mass as it calves into deeper and deeper water. In its retracted phase, Taku Glacier leaves behind a fjord that eventually becomes filled in with outwash sediments from Taku Glacier and fluvial sediments from the Taku River (*Nolan et al.*, 1995).

Taku Glacier most likely overlies thick sediments in the area of our 2016 seismic line. Radar data from *Motyka et al.* (2006) show that the glacier bed in the area of our 2016 survey lies from 45 m above the fjord bottom mapped in 1890 to 20 m below the 1890 surface. Bathymetry maps (*Post and Motyka*, 1995) show that the deposition rate in the area of our seismic line was $\sim 0.3\,\mathrm{m\,yr^{-1}}$ from 1890 to 1937. This would extrapolate to a 1750 fjord bottom elevation of $-100\,\mathrm{m}$.

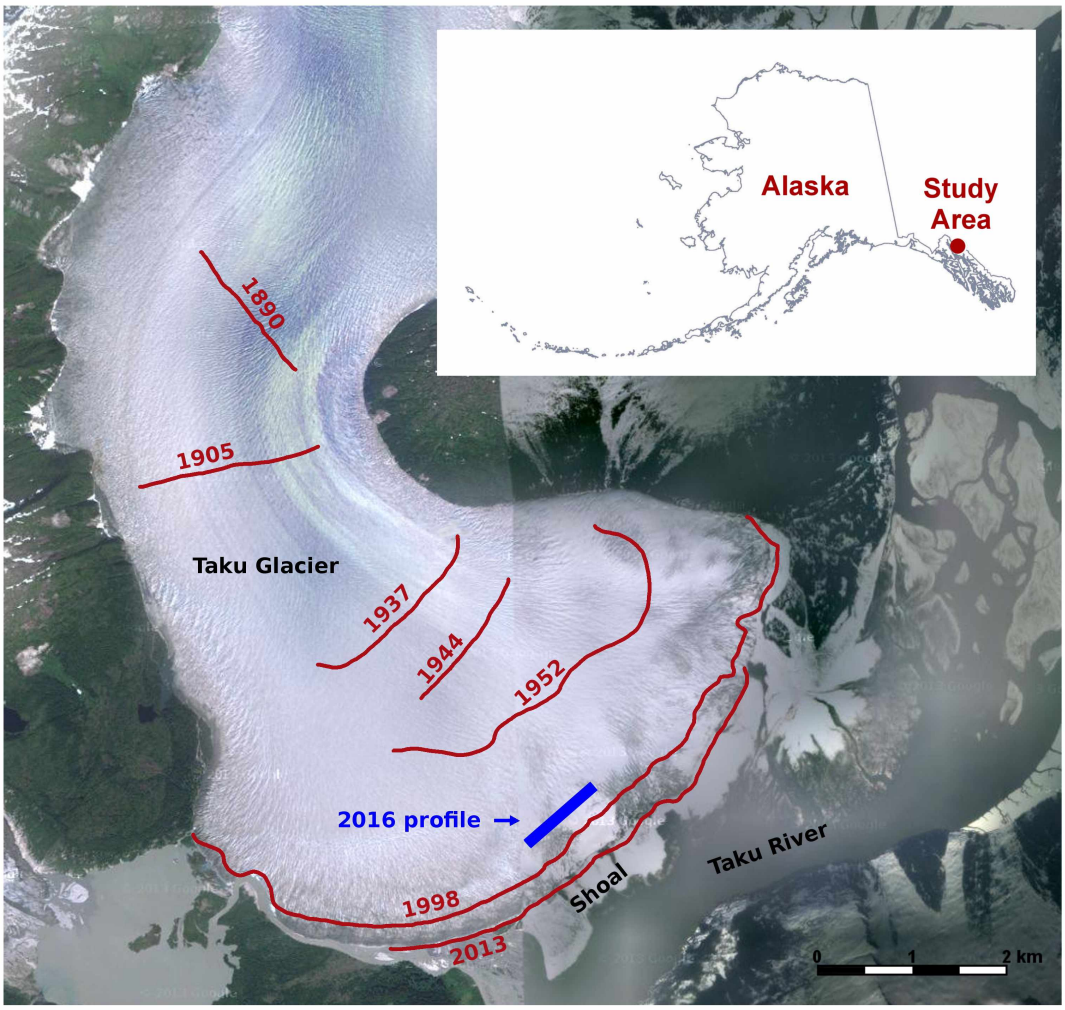

Figure 4: Taku Glacier terminus, showing the approximate location of the 2016 seismic survey. Historical terminus locations are shown in red (*Motyka et al.*, 2006). Imagery is from 2010 (Google Earth).

Assuming this, our seismic line is still >20 m above the 1750 fjord floor, which itself probably was not a bedrock surface. Marine seismic surveys in similar fjords show that the bedrock surface can be deeper than 300 m below sea level (*Post and Motyka*, 1995). If the same were true of Taku fjord, the bedrock would be at least 220 m below the glacier bed at the location of our seismic surveys.

2.2 Taku Glacier seismic experiment

To perform the seismic survey, we deployed 120 40 Hz geophones and 5 Geometrics Geode seismographs. We installed shots (120 g charges of Kinepak) at 10 m intervals along a line 930 m long. Shots were drilled 5 m below the glacier surface ($\sim$4 m into glacier ice). We buried geophones in vertical positions 1 m under the snow surface, spacing them 5 m apart along the southernmost 595 m of the shot line.

Our seismic measurements have shown that the ice depth increases to the north and varies from $\sim$160 m to 200 m. We obtained these values from an unmigrated stacked seismic image of normal-moveout-corrected common midpoint gathers with a divergence compensation gain applied. We performed these calculations using an ice velocity of 3640 m s^{-1}, calculated from the arrival times of the direct compressional wave. Based on these depths, the maximum source-receiver angle was $\sim$70°. Figure 5 shows the survey geometry and the shape of the glacier bed obtained from the stacked seismic image.

Ground roll contamination strongly affects bed reflections from traces up to 200 m (or 27° to 30° incidence angle) offset from the energy source (Figure 6). A few reversed-polarity bed returns are visible through the groundroll noise at near-normal offsets, and bed returns past 27° to 30° are not polarity-reversed. This negative polarity at small incidence angles indicates that the subglacial material is probably a dilatant till, though we cannot rule out a dewatered till as their normal incidence reflectivities can be positive or negative (see the dewatered till range in Figure 2).

2.3 Taku Glacier sediment samples

Small sediment samples recovered (using a gravity corer) in August 2015 from two boreholes at the site of the 2016 seismic survey were sandy clays with water contents of 15 % to 24 % and 16 % to 26 %. Sample densities could not be obtained, so the porosities of these samples are unknown. Upper porosity limits of 34 % to 45 % and 35 % to 47 % are calculated based on a solid fraction density of 2600 kg m^{-3}, a reasonable density for the local bedrock, which

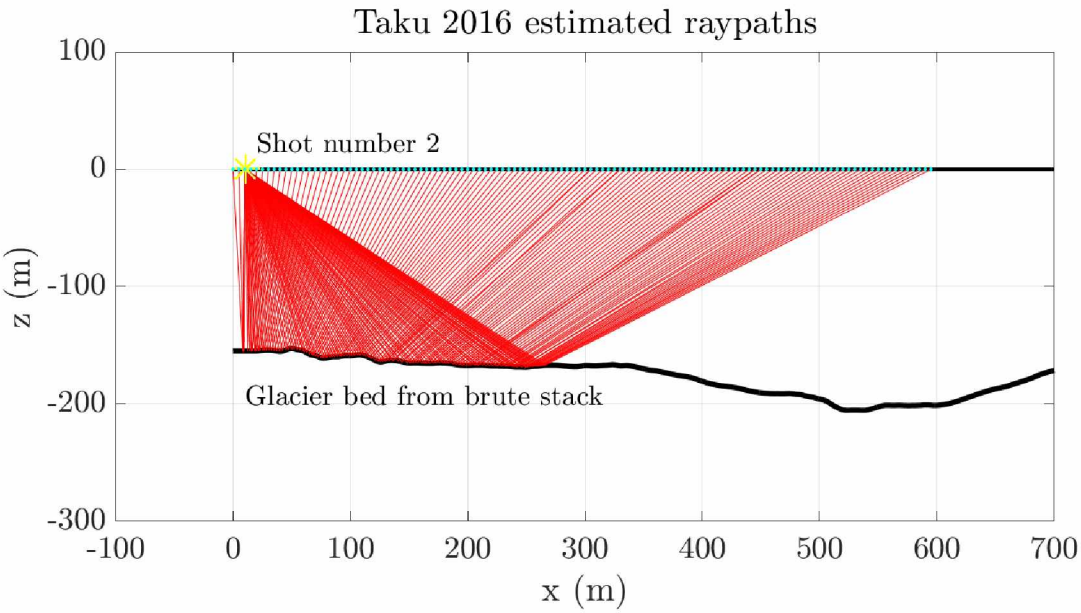

Figure 5: The 2016 survey geometry with ray tracing for one shot.

consists of tonalite (*Gehrels and Berg*, 1992). The large reported ranges for water content and porosity are from the possibility of water adhering to the gravity corer and samples during extraction. If no water was added in this way, then the upper values of these ranges are most representative of the water content. The sediment could also have experienced dewatering due to the gravity corer method (*Talalay*, 2013) to the effect that our range underestimates the sample porosity.

Our calculated porosity ranges indicate a dilatant till, though uncertainties allow a chance that the till is dewatered. The sample porosities could fall into the dewatered range if we unintentionally added water during the extraction process and/or overestimated solid fraction density.

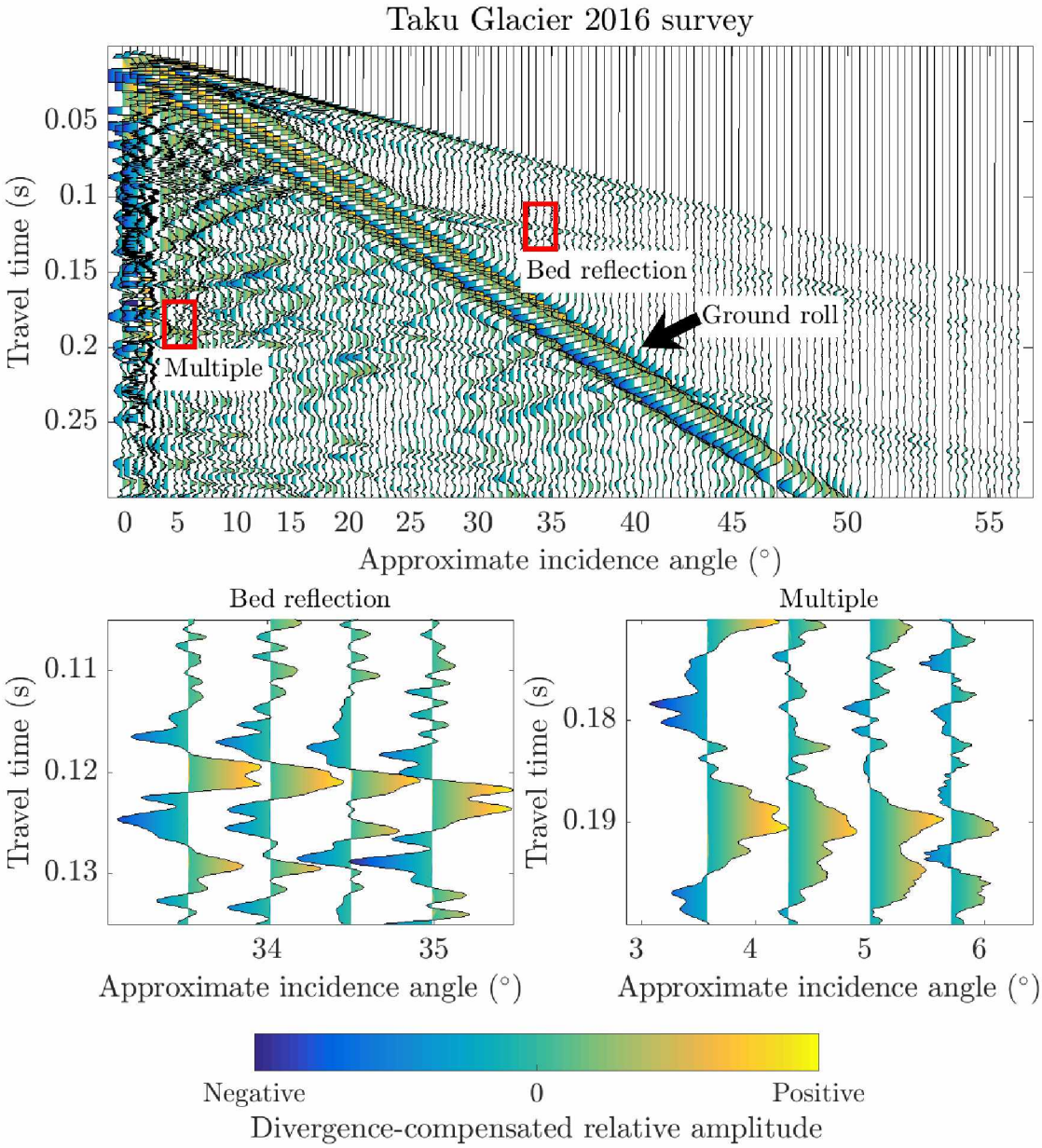

Figure 6: An example of a raw seismic record from the 2016 Taku survey. The bed reflection is visible before ground roll waves arrive. The left lower panel shows the bed reflection at $\sim 34°$ offset: the first half cycle of the wavelet has the same polarity as the direct wave. The right lower panel shows a signal that could be a normal-incidence bed reflection multiple, though wavelets are oddly-shaped due to groundroll interference.

3 An AVA forward model

In order to better understand the Taku Glacier data set, we first test AVA analysis methods on controlled synthetic datasets. This allows us to see how well physical till parameters can be recovered in the presence of noise typical of valley glaciers. We are also able to investigate the specific effects of different noise sources and processing techniques.

The forward model uses an input glacier bed, surface, and crevasse geometry, an input set of bed seismic parameters, an input seismic acquisition geometry, and an input source wavelet shape. This model assumes that the glacier ice has a uniform seismic velocity and there are no firn layers at the surface. We also assume that the subglacial material is uniform

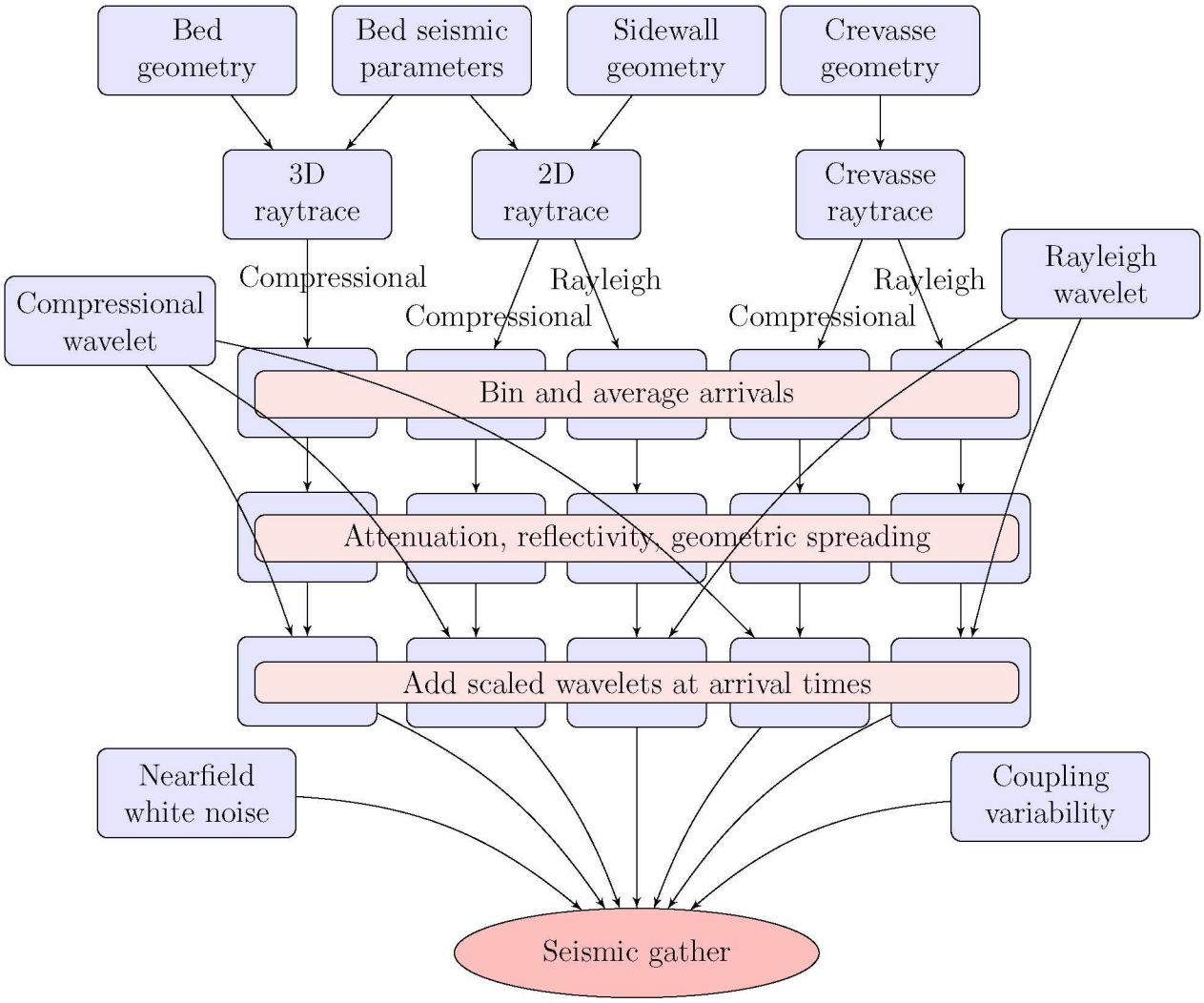

Figure 7: Flow diagram of the forward model.

and thicker than $\frac{1}{4}$ of the seismic wavelength, so that thin-layer effects do not distort the reflection wavelets (*Booth et al.*, 2012; *Widess*, 1973).

We choose some hypothetical values for Taku Glacier till seismic parameters: $\rho = 1800\,\mathrm{kg\,m^{-3}}$, based on a porosity of 50% and a solid fraction density of $2600\,\mathrm{kg\,m^{-3}}$, $\alpha = 1700\,\mathrm{m\,s^{-1}}$, and $\beta = 200\,\mathrm{m\,s^{-1}}$, which are all within the range of observed values in Table 1. These values also serve as forward model inputs.

Our model is a simple ray-tracer that does not solve the wave equation. Instead, signal types are assigned a source wavelet with an arbitrary 5 m offset amplitude. Wavelets are added to traces based on modeled arrival times. We correct their amplitudes for spherical spreading and bed reflectivity. A Zoeppritz equation script (*Krebes and Margrave*, 1991; *Aki and Richards*, 2002) calculates these bed reflectivities based on modeled incidence angle. The model also attenuates source wavelets using a frequency-dependent constant Q impulse response (*Kjartansson*, 1979; *Margrave*, 1999).

We use a 1 m digital surface model (DSM) of a deglaciated valley as a model input. We choose the Green Lakes Valley in the Colorado Front Range, which *Anderson* (2014) used to illustrate a typical lumpy glacier valley. Two lakes cause flat spots to appear in the DSM; we transform these into depressions. For the ice surface we use a parabolic sheet inclined by 2° with a glacier outline defined by the intersection of the ice surface with the digital surface model. The digital surface model (760 m by 1990 m) was resampled to 10 m resolution to conserve memory and computing power. We add a chevron pattern of crevasses at the glacier edges and flow-perpendicular crevasses at the glacier midpoint. Crevasses are spaced ~ 15 m apart. We find from satellite images (Google Earth) that valley glaciers tend to have crevasses spaced at ~ 10 m to 20 m intervals.

We base our choices for forward model parameters (wavelet shapes, relative amplitudes, frequencies, and anelastic attenuation values) on the 2016 Taku seismic data. The following describes how we arrived at these parameter values (listed in Table 3).

3.1 The source wavelet and its frequencies

In order to obtain frequencies to use in the forward model, we measure periods of direct waves, bed reflections, and Rayleigh waves in the first common shot gather from the Taku Glacier dataset. The start and end of the first cycle of the wavelet is chosen based on the first visible deviation from the trace background noise. We skip picking if these points are indistinguishable from background noise.

Wavelet frequencies decrease as they travel away from the source due to frequency-dependent attenuation, so we determine zero-offset frequencies to use for the source wavelets in the forward model. Since near-offset wavelets are clipped and suffer interference from other wavelets, we determine zero-offset frequency via linear regression from farther-offset wavelet period data.

We also require compressional wave and Rayleigh wave center frequencies to calculate attenuation in the forward model. The peaks of the amplitude spectra of stacked direct arrival and groundroll wavelets provide these.

Once we have obtained zero-offset frequencies, we construct source wavelets for compressional waves and Rayleigh waves. We assume a Berlage source wavelet shape (*Aldridge*, 1990), which is similar in appearance to arrivals in the Taku dataset (Figure 8). Compressional wave and Rayleigh wave source wavelets are different only in the input parameters to the Berlage wavelet, namely frequency, wave damping, and the number of nodes.

Random-looking noise in the source wavelet is also observed in the Taku dataset. We

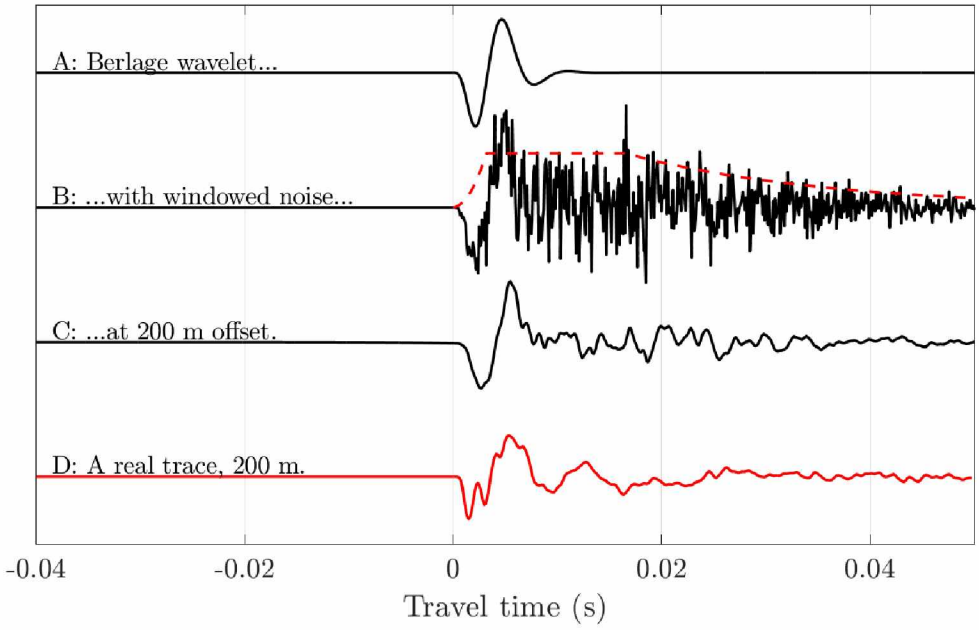

Figure 8: The Berlage source wavelet. A: The plain Berlage wavelet. B: The wavelet with windowed Gaussian-random noise added; the red dashed line shows the window shape. C: The same wavelet affected by a seismic quality factor impulse response to simulate anelastic attenuation from travel though 200 m of ice. D: A direct arrival wavelet from the Taku Glacier dataset, recorded 200 m from the shot.

believe that this noise is due to the bumpy and crevassed nature of the surface ice. To simulate this noise we add windowed white noise to the source wavelet. The noise window has zero amplitude at the start of the first arrival and ramps parabolically up to a maximum amplitude over the first wavelet half-cycle to remain constant for the next two periods. After that, its amplitude halves every two periods. Once we add the windowed white noise, we use a highpass filter (above 50 Hz) to demean the source wavelet.

3.2 Seismic quality factor

Seismic quality factor Q is the inverse of internal friction, a material property proportional to the fraction of energy a wave loses per cycle as it travels through a material. We require a value for Q to calculate seismic wave attenuation in ice. In AVA studies of ice sheets, Q is commonly given a value of ∼100–1000 (*Peters*, 2009). Temperate glaciers can have lower bulk Q values (65 for Athabasca Glacier according to *Clee et al.* (1969)) and still lower Q-values in near-surface ice (4–9 at Storglaciaren[3] according to *Gusmeroli et al.* (2010)). The reflectivity equation (Equation 12) is more sensitive to seismic quality factor when Q is small, because Q occurs in the denominator of the exponential term (Equation 11). Since we expect Q values in Taku Glacier ice to be low, we try to minimize uncertainty when we calculate seismic quality factor from the Taku Glacier data.

We calculate the seismic quality factor for Taku Glacier ice from the direct wave, using the spectral ratio method (*Gusmeroli et al.*, 2010). First we form common offset gathers of all available traces, and stack them. We extract stacked first arrival wavelets using a Tukey window with tails 10 % of the wavelet length and determine the spectral amplitudes of the wavelets. $\ln \frac{S_0}{S_1}$ is plotted against frequency, where S_0 is the spectral amplitude of the nearest-offset wave and S_1 is the spectral amplitude calculated from waves at greater offsets. We obtain S_0 from the first direct wavelet that does not suffer amplitude clipping or groundroll interference.

The slope of $\ln \frac{S_0}{S_1}$, γ, is related to Q as follows:

$$\gamma = -\frac{\pi \Delta t}{Q}, \tag{3}$$

where Δt is the traveltime difference between the two wavelets from which S_0 and S_1 were obtained.

[3]Storglaciaren surface ice was −1 °C (*Gusmeroli et al.*, 2010). Lower Q values would be expected for temperate surface ice.

Q can be approximated as a constant over narrow frequency ranges, but over larger ranges Q is frequency-dependent. We choose to calculate Q within a frequency range where the spectral amplitude is at least 50% of the maximum. Over this range, we must find a linear fit to $\ln \frac{S_0}{S_1}$ versus frequency. Fortuitously, this coincides with a region where the $\ln \frac{S_0}{S_1}$ versus frequency has a nearly constant slope.

We find that the seismic quality factor varies with shot offset, first increasing and then leveling off. This reflects the lower Q-values that the shorter rays experience. Rays are affected by the ice within their elliptical Fresnel zones, to the effect that longer rays sample deeper ice with higher Q-values. Seismic quality factor decreases with degree of material fracture, unless the material is fully saturated with water. Thus, we can expect a glacier surface to have low seismic quality factor values, with Q increasing with depth (*Gusmeroli et al.*, 2010; *Babcock and Bradford*, 2014) as voids in the ice become smaller and more water-saturated.

In order to find the seismic quality factor of the deeper ice using the direct wave data, we create a forward model to calculate the average seismic quality factor, Q_a, in the Fresnel volume. We assume that the ice thickness is divided into a lower layer where seismic quality factor is constant (Q_i) and an upper layer of thickness $c = 30\,\mathrm{m}$ (equal to the maximum vertical extent of crevassing) where Q_z (depth-dependent seismic quality factor) increases linearly from a surface value (Q_s) to Q_i. This is equivalent to a power-law decrease in internal friction, a material property equal to Q^{-1}.

$$Q_\mathrm{z} = \begin{cases} Q_\mathrm{s} + \left(\dfrac{Q_\mathrm{i} - Q_\mathrm{s}}{c}\right) z, & 0 \leq z < c \\ Q_\mathrm{i}, & z \geq c \end{cases} \tag{4}$$

The average seismic quality factor Q_a of the Fresnel zone is calculated by numerically integrating Q_z over the Fresnel zone volume and dividing by total Fresnel zone volume V_t:

$$Q_\mathrm{a} = \frac{1}{V_\mathrm{t}} \sum_{z=0}^{r} Q_\mathrm{z} A \Delta z, \tag{5}$$

where

$$V_\mathrm{t} = \sum_{z=1}^{r} A \Delta z. \tag{6}$$

Above, r is the Fresnel zone radius (Equation 7), A is the area of the slice of Fresnel zone

at depth z (Equation 8), and Δz is the thickness of the depth interval. We use $\Delta z = 1\,\mathrm{m}$.

$$r = \frac{1}{2}\sqrt{R\lambda} \tag{7}$$

$$A = \left(\frac{L}{2}\right)\left(\frac{l}{2}\right)\pi \tag{8}$$

In Equation 7, λ is the wavelength of the seismic ray, and R is half the shot-geophone distance. L in Equation 8 is the major axis of an ellipse that represents the horizontal slice of the Fresnel volume ellipsoid and l is the minor axis of the ellipse.

The ellipse axes L and l are found from

$$L = \frac{d}{R}\sqrt{R^2 - z^2} \tag{9}$$

and

$$l = 2\sqrt{r^2 - z^2}. \tag{10}$$

We fit Equation 5 to the Taku direct wave Q (outliers removed), inverting for the seismic quality factors of the deep ice and the surface ice using a least-squares grid search. The grid search returns $Q_\mathrm{s} = 30$ and $Q_\mathrm{i} = 170$. These values, when used in our Q_a forward model, provide a reasonable fit to our observations.

Generally to find the average seismic quality factor, one must actually perform the averaging over internal friction Q^{-1}, then take the inverse of the result. We test the inversion using this averaging method, which results in a very poor constraint on Q_i; Q_i goes to infinity as Q_s approaches zero, and the only way to constrain Q_i is to assume a value for Q_s. Consequentially we elect to average over Q, which results in a misfit function with a well-defined minimum. We deem this acceptable because only for small values of Q_a ($Q_\mathrm{a} << 100$) will Q_a innacuracies have a significant impact on the AVA process.

The Q-value of the groundroll (Q_r) is also calculated following the spectral ratio method. We found Q_r to have little offset dependence. Thus we use a constant seismic quality factor when we calculate Rayleigh wave attenuation ($Q_\mathrm{r} = 12$).

Table 3: Constants used in the forward model

	Model input	value
α_i	Compressional wave speed in ice	$3700\,\mathrm{m\,s^{-1}}$
β_i	Shear wave speed in ice	$1850\,\mathrm{m\,s^{-1}}$
ρ_i	Density of ice	$917\,\mathrm{kg\,m^{-3}}$
α_till	Compressional wave speed in till	$1700\,\mathrm{m\,s^{-1}}$
β_till	Shear wave speed in till	$200\,\mathrm{m\,s^{-1}}$
ρ_till	Density of till	$1800\,\mathrm{kg\,m^{-3}}$
V_r	Rayleigh wave velocity	$1700\,\mathrm{m\,s^{-1}}$
Q_s	Seismic quality factor of the surface ice	30
Q_i	Seismic quality factor of the deep ice	170
Q_r	Seismic quality factor for Rayleigh waves	12
c	Depth at which seismic quality factor stops increasing	30 m
f_p	Center frequency for the compressional wave	100 Hz
f_p0	Starting frequency for the compressional wave	150 Hz
f_r	Center frequency for the Rayleigh wave	50 Hz
f_r0	Starting frequency for the Rayleigh wave	60 Hz
c_r	Crevasse 'reflectivity'	0.3
dt	Sampling interval	0.0001 s
Δz	Integration increment for calculating Q	1 m
x_0	Offset where a signal amplitude is the reference amplitude	5 m
a_rr	Reflected wave reference amplitude	1000
a_rd	Direct wave reference amplitude	100
a_rg	Groundroll reference amplitude	2000
a_random	Gaussian-random noise average amplitude	0.0002
a_wp	Relative amplitude of the compressional wave white noise	1/2
a_wr	Relative amplitude of the Rayleigh wave white noise	1/4
a_c	Ratio between trace amplitude and shot coupling variability	5
n_p	Number of nodes in the compressional wave source wavelet	3
n_r	Number of nodes in the Rayleigh source wavelet	4
α_p	Compressional-wave source wavelet damping term	950
α_r	Rayleigh-wave source wavelet damping term	180

3.3 Reflection raytracing

We start the forward modeling process by choosing a location for our seismic survey on the input glacier surface. The desired range of ray incidence angles determines the width of the seismic line, based on the ice thickness at the center of the seismic line. The desired fold of coverage determines the spacing of shots and receivers. For simplicity, shots coincide with receiver locations.

We construct bed reflections using a two-layer raytracing algorithm with a 3D layer interface. Rays emanate from the seismic source towards the glacier bed. To ensure a ray density that is close to uniform, we generate a large number of rays (5000) in random directions. For each ray, the model fits a plane to the subset of bed points that lay in the ray Fresnel zone. The reflected ray vector is calculated from the plane and incident ray, and the reflected ray is traced back to the surface. Rays that emerge near geophones provide ray travel times and bed incidence angles. If the search returns multiple rays for a given geophone, it bins the rays by bed incident location and averages the ray arrival times so that only one arrival per bin is recorded. If no rays are returned to a geophone within the search radius, the nearest surface-incident ray is chosen.

We then produce the reflection wavelet scaled by bed reflectivity, geometric spreading, and anelastic attenuation. Since bed reflected rays interact with all layers of ice, we calculate a bulk average Q-value using Equation 4.

A bed reflection multiple is modeled by continuing to trace the surface-incident ray to the glacier bed again and back to the surface. We record the longer travel time and transform the multiple wavelet based on Q and spherical spreading accordingly. We also scale the wavelet by the product of the reflectivities of its two reflections with the bed and its reflection with the surface. Since we only use near-normal-offset multiples in AVA analysis, we assume that the reflectivity of the ice/air interface is -1 (see Figure 2).

3.4 Reflections from surface features

The model includes backscattered signals from crevasses when it calculates direct wave and Rayleigh wave arrivals. Backscattered direct waves and surface waves are clearly visible in the Taku seismic data (see Figure 6).

We calculate the general 'reflectivity' c_{r} (proportion of backscattered vs. transmitted energy, converted to amplitude) of crevasses using backscattered signals observed in the Taku dataset. To calculate crevasse reflectivity, we measure the amplitudes of wavelets both

before and after each scattering event in the first common shot gather of the Taku dataset, as well as the amplitudes of the backscattered wavelets. These reflectivities vary from 0.1 to 0.6. A c_r value of 0.3 is chosen to represent an average, and we hold it constant for every crevasse reflection in the model regardless of incident angle or crevasse size. Note that in reality c_r depends on the ray incident angle with the crevasse and the size of the crevasse relative to the wave Fresnel zone (*Benjumea and Teixidó*, 2001); we ignore these considerations because our c_r is just a crude approximation of highly variable values.

We determine Rayleigh and direct wave arrival times using a 2D raytracing model with crevasse endpoint locations as inputs. 1000 rays leave the seismic source in uniform directions. Every time a ray intersects a crevasse, a ray reflects off the crevasse and may intersect a geophone, while a second ray is transmitted past the crevasse. The amplitude of the ray that propagates past the crevasse is equal to $\sqrt{a_\mathrm{i}^2 - (c_\mathrm{r} a_\mathrm{i})^2}$, where a_i is the amplitude of the incident ray. The amplitude of the reflected ray is $c_\mathrm{r} a_\mathrm{i}$.

This doubling of rays at every crevasse leads to a very large number of rays in the model. We avoid this problem by choosing to either reflect or transmit one ray past each crevasse, rather than to continue both the reflected and transmitted rays. This choice is made based on the following criteria: if a ray is directed towards a geophone, it is transmitted past the crevasse. Otherwise, it reflects off or propagates past the crevasse with equal probability. Each ray is only allowed to reflect up to 9 times, after which its amplitude is considered negligible ($\sim 2 \cdot 10^{-5}$ times the source amplitude even before accounting for attenuation from Q or geometrical spreading).

In addition, extra rays are propagated along the geophone line and reflect once off every line-intersecting crevasse. This ensures that all geophones have the opportunity to pick up at least two generations of direct and Rayleigh waves: a ray traveling straight from the source, as well as a singly-reflected ray.

Rayleigh waves and direct compressional waves also reflect off of glacier sidewalls. We use a 2D adaptation of the 3D raytracing algorithm to produce sidewall reflections. Rayleigh wave reflectivity is set to c_r for simplicity, while direct wave reflectivity is determined via the Zoeppritz equations and the assumption that the sidewall material is identical to the basal material.

Arrivals from sidewall and surface reflections are sorted in the same way as the bed arrivals. We add scaled Berlage wavelets according to modeled arrivals times, and correct the wavelets for spherical spreading and attenuation due to Q_a of the wave Fresnel zone.

3.5 Seismic record assembly

Bed reflections, sidewall reflections, primary waves with crevasses, and Rayleigh waves with crevasses are calculated separately. They can simply be added together to produce the final seismic record. Very low amplitude nearfield white noise is added to this record to add further realism to the model. Finally, we simulate variability in shot-geophone coupling by multiplying each trace by a factor chosen at random between 0.6 and 1.0.

4 Amplitude Variation with Angle analysis

Once we produce a synthetic seismogram, we perform AVA analysis of it using the following procedures (outlined in Figure 9)

4.1 Incidence angle and depth

A normal moveout correction is applied to the model results, using an ice velocity calculated from the first breaks of the stacked direct wave. Common-midpoint gathers are stacked to

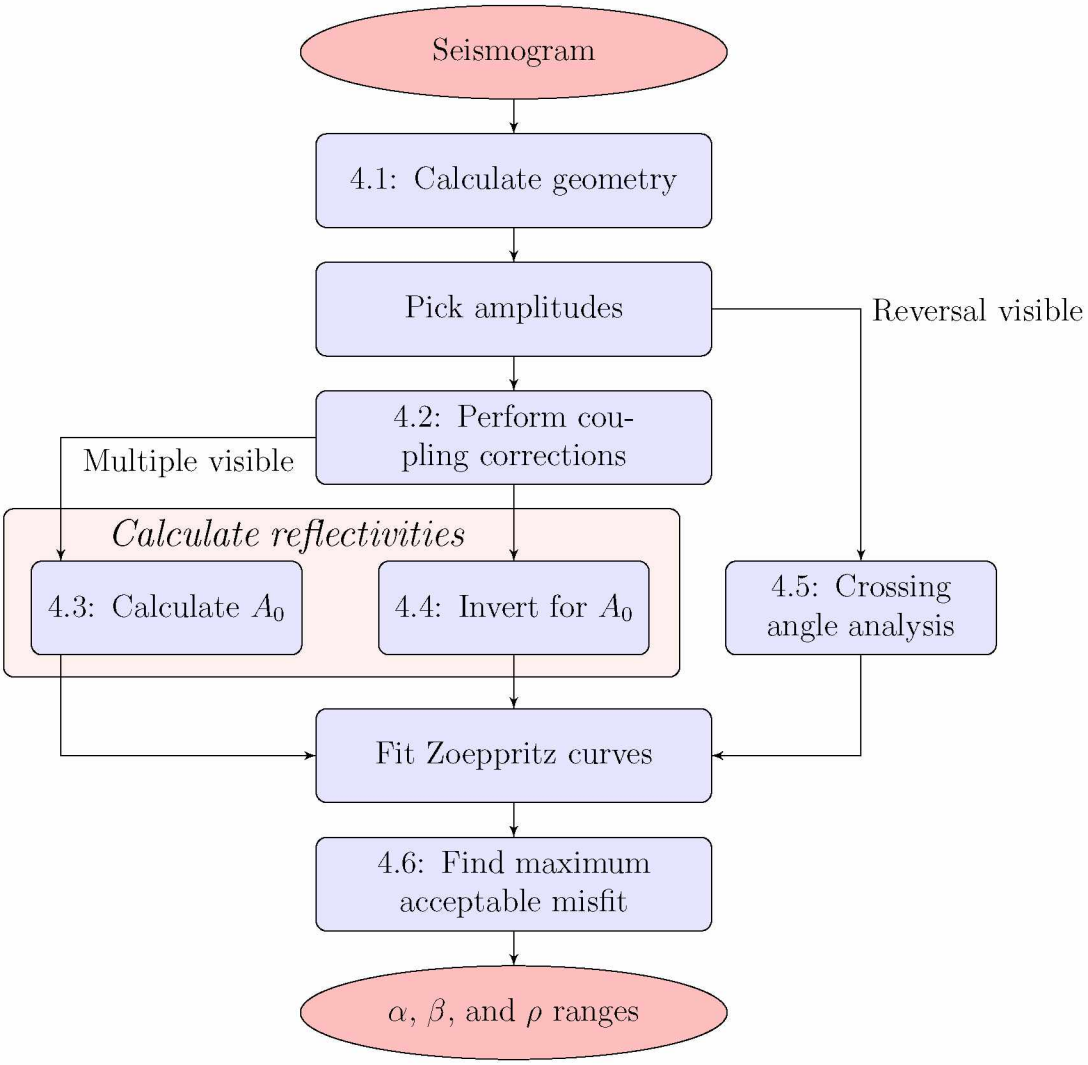

Figure 9: Steps taken to complete AVA analysis. Numbers refer to the section and subsection where each procedure is described.

produce a seismic image. We assume that the first breaks of the stacked section represent the bed cross section directly under the seismic line. Incidence angles and locations for each reflected wave are derived from a forward model of raypaths using this bed shape.

4.2 Shot-geophone coupling

We determine the root-mean-squared amplitudes of the direct arrival wavelets. Amplitudes are corrected for spherical spreading by multiplying by x^{-1}, where x is the direct wave raypath length. Direct waves are also multiplied by e^{ax} to correct for anelastic attenuation. a is found from

$$a = \frac{\pi f}{\alpha_{\text{ice}} Q_{\text{a}}}, \tag{11}$$

where α_{ice} is the compressional wave velocity of the ice and f is the dominant frequency of the wavelet. We determine Q_{s} and Q_{i} from the synthetic data using the same process we employed with the 2016 Taku data, and find Q_{a} for each direct wave using Equation 5.

Attenuation-corrected direct wave amplitudes are normalized to their average, and these normalization factors are assumed to correct for shot-geophone coupling variability. We multiply the amplitudes of each raw trace by its corresponding entry in the normalization vector.

4.3 The reflectivity curve

We pick the amplitudes of the bed reflection wavelets and near-offset bed reflection multiple wavelets. With these amplitudes and raylengths and with source amplitude A_0, we can calculate bed reflectivity R using:

$$R = \frac{A_1}{A_0\,\gamma}\, e^{ax}, \tag{12}$$

where A_1 is the bed reflection amplitude, x is the raypath length, and a is calculated from Equation 11 using the average Q-value of the entire ice thickness and the center frequency of the bed reflection. The factor γ is a geometrical correction term (Equation 13),

$$\gamma = \frac{1}{x}\cos(\theta) \tag{13}$$

where θ is the angle (from vertical) at which the seismic wave reaches the receiver.

We calculate A_0 using

$$A_0 = \frac{{A_1}^2 x}{2A_2} \tag{14}$$

from *Peters* (2009), where A_2 is the amplitude of the bed reflection multiple. Equation 14 requires that A_1 and A_2 are derived from the same normal-offset trace.

We use raw primary and multiple amplitude picks from the closest non-zero-offset traces to find source amplitude A_0. Ideally zero-offset traces would be used, but we find these to be poor quality due to proximity to the shot.

The reflectivity of every wavelet is calculated using Equation 12 and Equation 14. These reflectivities yield the AVA curve when plotted against incidence angle. We invert for ρ, α, and β using a grid search to find the best Zoeppritz curve fit in the least-squares sense. Grid search spacing is $\Delta\alpha = 20\,\mathrm{m\,s^{-1}}$, $\Delta\beta = 20\,\mathrm{m\,s^{-1}}$, and $\Delta\rho = 20\,\mathrm{kg\,m^{-3}}$.

The grid search is restricted to parameter combinations that are physically plausible. α, β, and ρ combinations must lay within the range of a dilatant till, a dewatered till, or a consolidated till (see Table 2 for acceptable ranges). Combinations are rejected if seismic parameters disagree on a till type–for example if ρ is too low to be a dewatered till, yet β is too high to be a dilatant till. Such regions of the grid search are given values of NaN and appear as blank areas in grid search plots. Once we have determined best fit seismic parameters from our constrained minimization, we report deviations from the model input values.

To see if it improves results, we also test the use of a frequency bandpass filter with a lower cutoff of 60 Hz, a plateau between 120 Hz and 300 Hz, and a higher cutoff at 600 Hz. Such a filter has worked well to reduce groundroll noise in the Taku 2016 dataset.

4.4 Inverting for the source amplitude

We attempt performing AVA without the bed reflection multiple by following the methods of *Dow et al.* (2013). For every combination of α, β and ρ, we compare the modeled Zoeppritz curve with simulated reflectivity curves calculated from the bed reflection amplitudes (binned by incidence angle) and a range of possible A_2 values. The tested range of A_2 values are equally spaced from zero to half of a reference A_1 value. This reference amplitude is equal to the normal-incidence reflection amplitude, or, if that is not available, the maximum reflection amplitude. We use the range of A_2 values to calculate corresponding A_0 values using the reference reflection amplitude and Equation 14. We discard the highest A_0 value, which is infinity. Next we calculate simulated reflectivity curves from each A_0 value.

Simulated AVA curves are rejected if normal incidence reflectivity exceeds 0.6 (the maximum for any type of ice/bed interface), or if the absolute value of reflectivity for any angle exceeds 1. To allow for some data error, we add a buffer of 0.1 to both of these values. We calculate simulated curve-modeled curve misfits and assign the smallest misfit to the grid cell for the tested α, β, and ρ combination.

4.5 Crossing angle analysis

Anandakrishnan (2003) estimated seismic parameters using reflectivity crossing angle, and we test their methods here. A grid search finds α, β and ρ based on the angle at which the phase reversal occurs.

The advantage of crossing angle analysis over A_2 inversion is that no reflectivity curve fitting is required. In A_2 inversion, incorrect calculation of attenuation alters the curve shape and changes the results. Crossing angle analysis avoids this problem, and furthermore allows us to skip Q calculation and coupling correction.

Crossing angle analysis is complicated by the fact that different AVA curves can have one, two, or no zero crossings. We stack raw amplitudes into 5° angle bins before finding zero crossings, which reduces the risk of finding a spurious zero crossing resulting from picking error. However, the process of binning could obscure a late-arriving zero crossing due to the effect of averaging. Consequentially, we reject forward models of AVA curves that do not reproduce an identified zero crossing, but we accept curves that produce too many crossings.

In the crossing angle inversion process we define the misfit as the gap between the observed and calculated crossing angles. We also define the maximum acceptable misfit as either the width of an angle bin or, if angle bins adjacent to the crossing are empty, half the width of the gap plus the width of an angle bin.

4.6 Acceptable misfit

In order to characterize an acceptable range of till parameter combinations (α, β, and ρ) in AVA analysis (crossing angle analysis excluded), we calculate an envelope of acceptable Zoeppritz curve fits. To fall within the envelope, Zoeppritz curves must satisfy a maximum acceptable misfit value $E_{\max}$.

Note that we do not perform a rigorous data error analysis here, as the nature of coupling corrections and reflectivity calculations in AVA results in errors that are systematic and non-Gaussian. The maximum misfit value $E_{\max}$ is determined from the best fit Zoeppritz

curve and the maximum data residual as follows.

The best-fit curve misfit (our minimum misfit $E_{\rm min}$) is equal to the sum of squares of the differences between the observed reflectivities $R_{\rm d}$ and the best-fit curve $R_{\rm m}$:

$$E_{\rm min}^2 = \sum_{i=1}^{n} \left(R_{\rm d}(i) - R_{\rm m}(i)\right)^2 . \tag{15}$$

Here, n is the number of datapoints.

We now find the maximum residual, h, in the dataset,

$$h = \max\left(|R_{\rm d}(i) - R_{\rm m}(i)|\right), \tag{16}$$

then we shift the best-fit curve up by h (approximating the top of our envelope) and re-calculate the misfit (Equation 17). We then define a maximum acceptable misfit as

$$E_{\rm max}^2 = \sum_{i=1}^{n} \left(R_{\rm d}(i) - R_{\rm m}(i) + h\right)^2 . \tag{17}$$

Multiplying the terms in Equation 17, we obtain

$$E_{\rm max}^2 = \sum_{i=1}^{n} (R_{\rm d}(i) - R_{\rm m}(i))^2 + \sum_{i=1}^{n} (R_{\rm d}(i) - R_{\rm m}(i))h + nh^2. \tag{18}$$

Assuming that the middle term is negligible because

$$\sum_{i=1}^{n} R_{\rm d} \approx \sum_{i=1}^{n} R_{\rm m}, \tag{19}$$

Equation 18 reduces to

$$E_{\rm max}^2 = \sum_{i=1}^{n} (R_d(i) - R_m(i))^2 + nh^2 = E_{\rm min}^2 + nh^2. \tag{20}$$

We now examine the results from our grid search over α, β, and ρ, and designate all combinations with misfits smaller than $E_{\rm max}$ as acceptable.

5 Results

We perform five model runs which are distinguished from one another by a combination of input geometry and AVA processing method. Model runs are listed in Table 4.

Table 4: Model runs.

Run name	Bed geometry	Crevasses	AVA method
Flat	Flat, 400 m deep	None	A_0 inversion
GL-long	Green Lakes, longitudinal	Perpendicular to survey	A_0 inversion
GL-trans	Green Lakes, transverse	Parallel to survey	A_0 inversion
$Flat_{\mathrm{A0}}$	Flat, 400 m deep	None	Calculate A_0
$Flat_{\mathrm{cross}}$	Flat, 400 m deep	None	Crossing angle

5.1 Deep, flat glacier run ('*Flat*')

In the *Flat* model (Figure 10), the bed reflection and the multiple are easily identified (Figure 11), and it is possible to complete a full AVA analysis. This returns seismic parameters that are close to the input parameters (see Figure 12) and lie within dilatant till ranges. Acceptable α and ρ ranges span the dilatant till parameter space, but β is well-constrained and ranges from $60\,\mathrm{m\,s^{-1}}$ to $200\,\mathrm{m\,s^{-1}}$. The possible curves envelope does not fully encompass the input parameter curve, however (Figure 13), which indicates that the source amplitude calculation underestimated the real source amplitude.

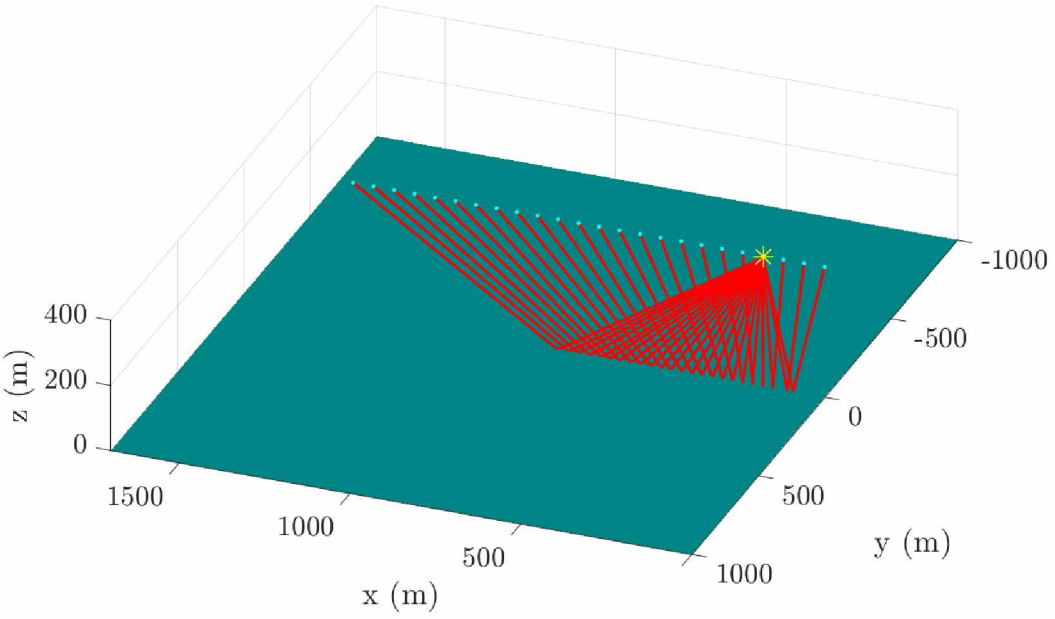

Figure 10: *Flat* survey setup. The glacier bed is flat and 400 m deep. Red lines indicate ray travel paths. The asterisk represents the seismic source location, and the points represent receivers. The survey consists of 24 shots total (coincident with receivers), though only one shot is shown in this figure.

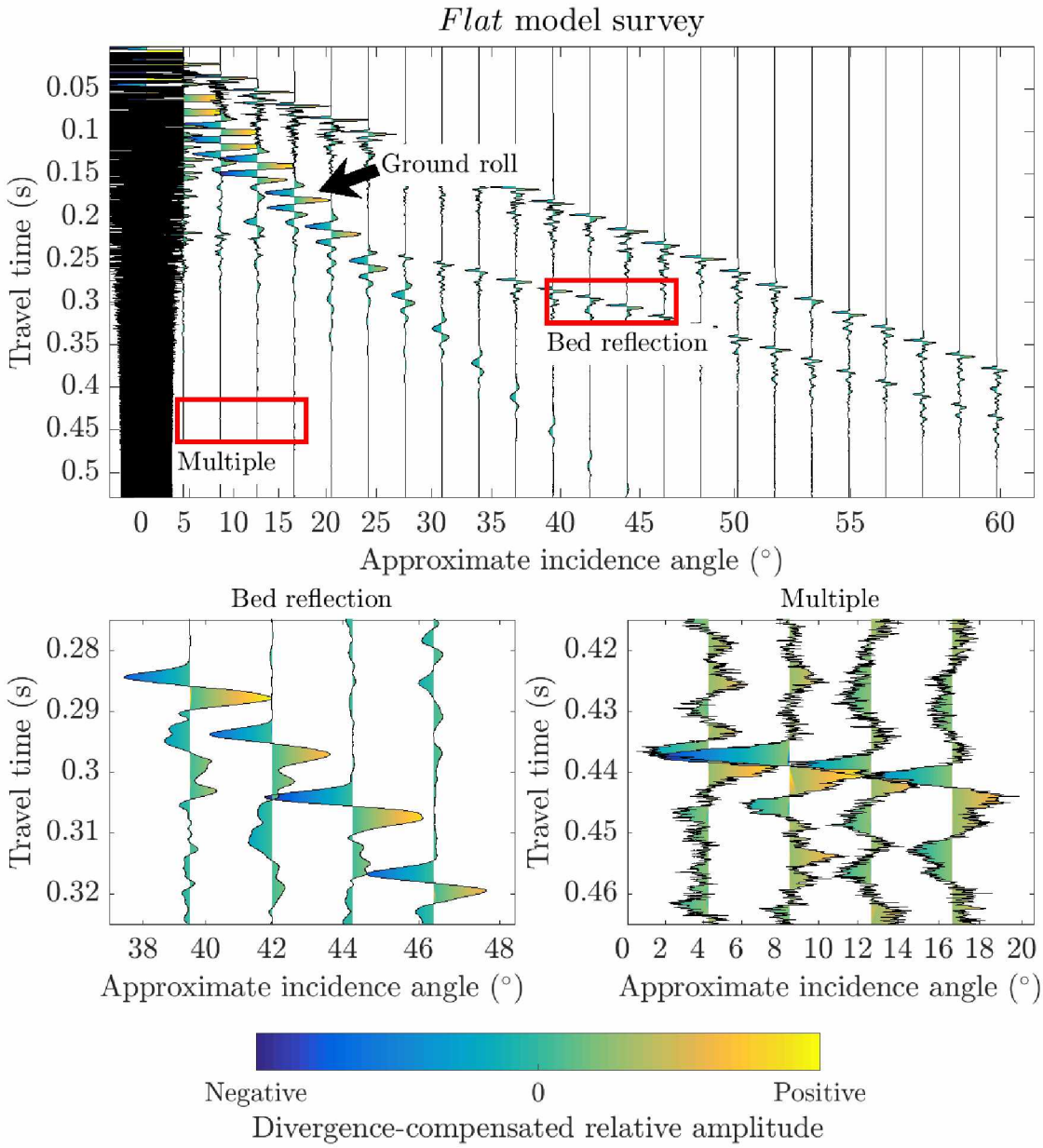

Figure 11: The first common shot gather of the *Flat* survey. The bed reflection is easily visible (left lower panel) as is its multiple (right lower panel). The seismic record is not shown in its entirety; it consists of 24 such gathers.

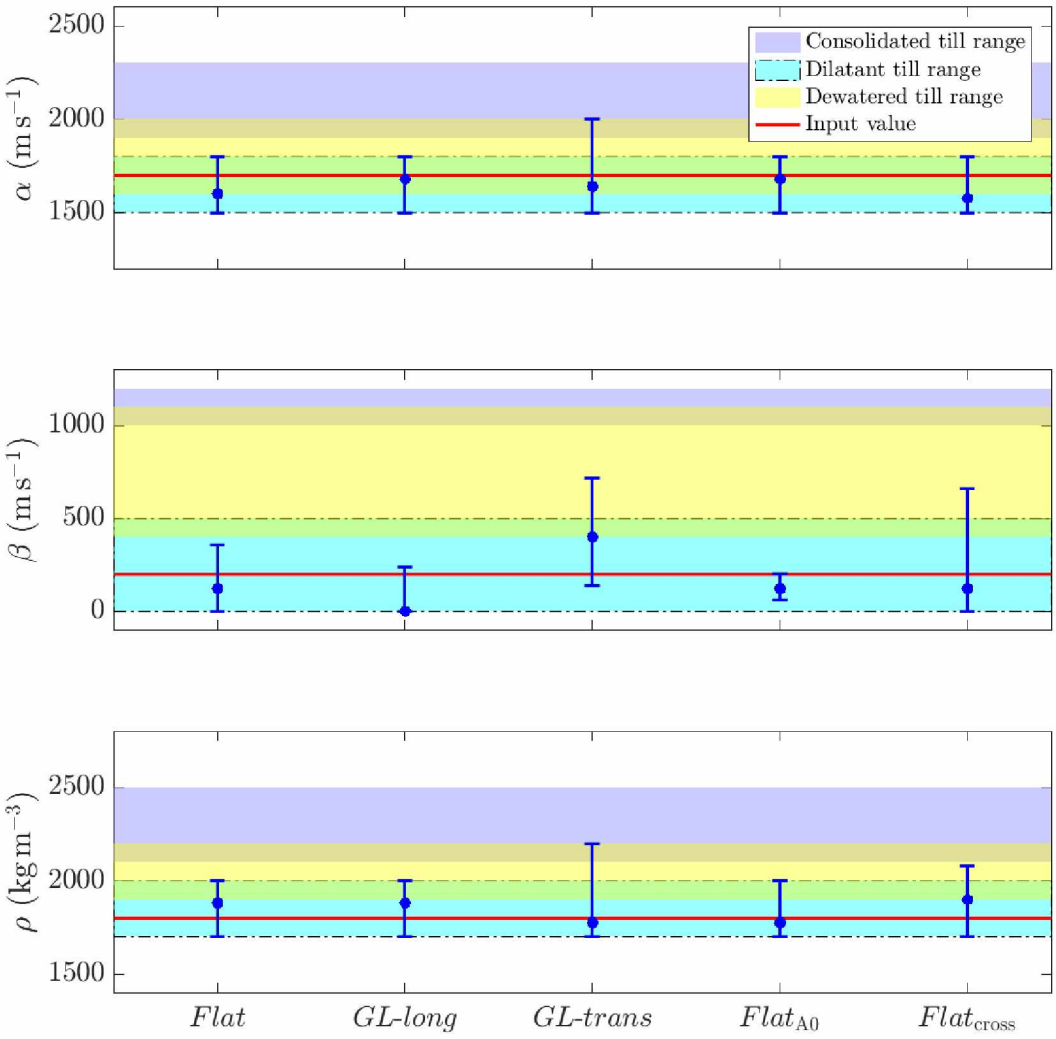

Figure 12: Parameter ranges returned by model runs, showing best fit values (dots) and acceptable ranges (whiskers)

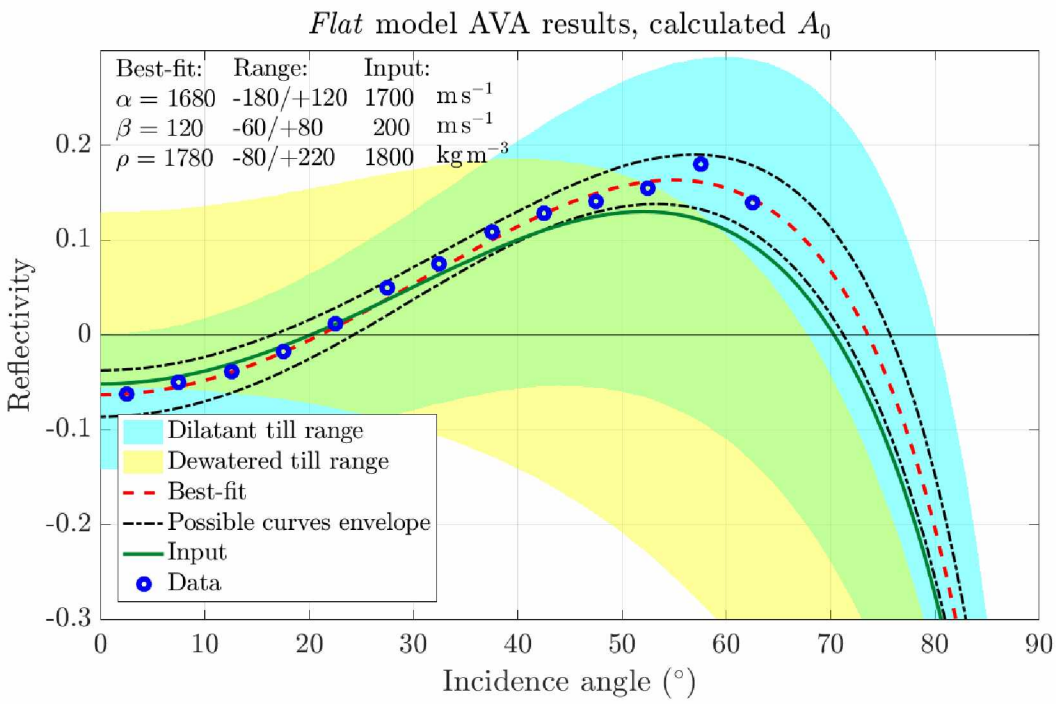

Figure 13: *Flat* AVA curve fit. A_0 is calculated from multiples. The blue circles are reflectivity averages within incidence angle bins, and represent data from all 24 shots.

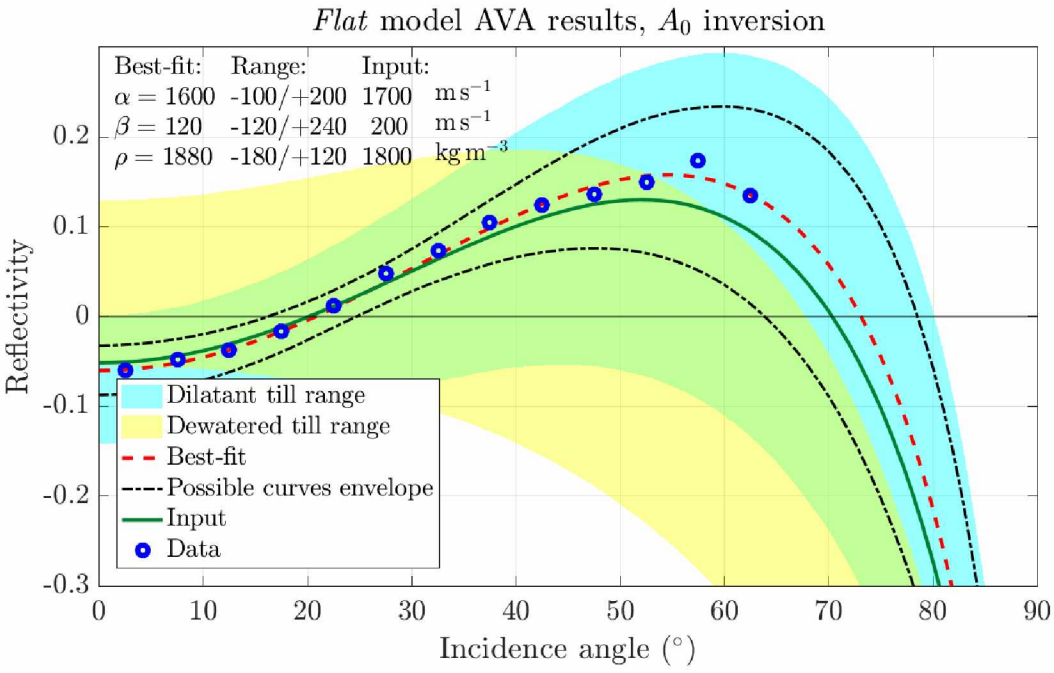

Figure 14: AVA curve fit to *Flat* data using source amplitude inversion.

Inverting for A_0 during AVA analysis also results in seismic parameter calculations in the dilatant till range, though β has a larger range and the possible curves envelope is also larger. When we invert for the crossing angle only (Figure 15), a large number of seismic parameter combinations can explain our results, including combinations in the dewatered till range.

Both AVA and source amplitude inversion of the *Flat* model run results reliably characterize seismic parameters. Misfit functions for the two techniques, however, look different from one another. Traditional AVA produces a misfit function with a well-defined minimum, resulting in a narrow solution range (Figure 16). A_0 inversion also results in a well-defined, but somewhat broader minimum (Figure 17).

Crossing angle analysis allows some parameter combinations that lay in the dewatered till range. Figure 18 shows that the crossing angle method yields misfit plots that do not center on a local minimum, but rather a trough. The relationship between α and β is well-constrained, but there is little variation in misfit value along that line.

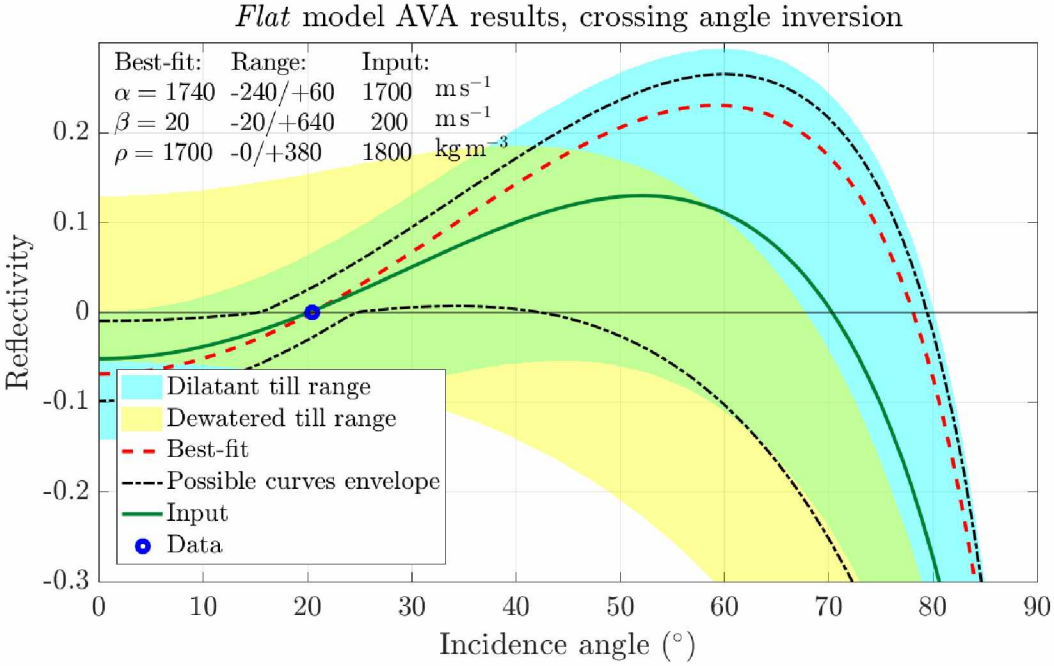

Figure 15: *Flat* AVA curve fit based on polarity crossing angle. The possible curves envelope encompasses all of the modeled curves that cross within 5° of the observed crossing angle.

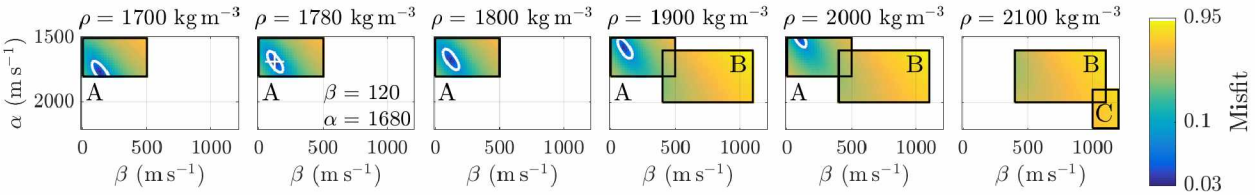

Figure 16: *Flat* AVA misfit (the square root of the sum of squares) plots. A_0 is calculated from the multiple. We calculate misfits for density values ranging from 1700 kg m^{-3} to 2500 kg m^{-3} and divided into 20 kg m^{-3} increments, but only some of the parameter space is shown. The white cross marks the best-fit seismic parameter combination, and the white contour encompasses all parameter combinations within the acceptable misfit range according to Equation 20. Misfits are only found for combinations of seismic parameters that fall into dilatant, dewatered, or consolidated till ranges. Block A represents the dilatant till range, block B encompasses the dewatered till range, and block C contains the consolidated till range. The colorscale is logarithmic.

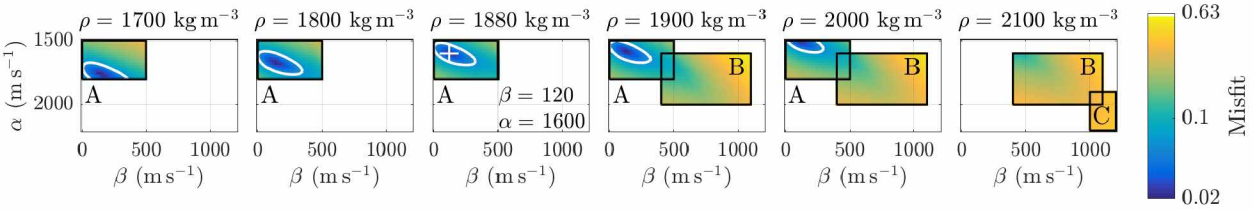

Figure 17: *Flat* AVA misfit: A_0 inversion. A, B, and C indicate the dilatant, dewatered, and consolidated till ranges, respectively.

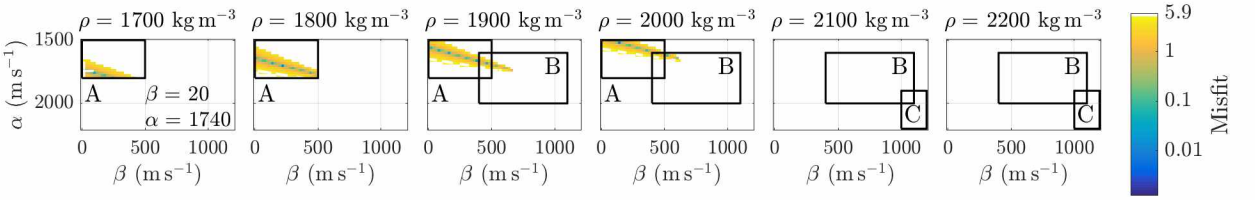

Figure 18: *Flat* AVA misfit: crossing angle inversion.

5.2 Longitudinal Green Lakes Valley run ('*GL-long*')

This model run uses the Green Lakes Valley geometry and a seismic line that is parallel to the glacier axis and perpendicular to crevasses (Figure 19). The survey samples a relatively flat part of the glacier bed (Figure 20), keeping the raypaths simple. In the output seismic gathers (see Figure 21 for an example), the multiple is obscured and so is part of the bed reflection. However, the visible parts of the bed reflection have high signal-to-noise ratios. A crossing angle cannot be determined, so we must invert for multiple amplitude. Multiple amplitude inversion in this case yields parameters that lie only within the dilatant till range (Figure 22). The misfit plot places additional constraints on β (it must be $<240\,\mathrm{m\,s^{-1}}$).

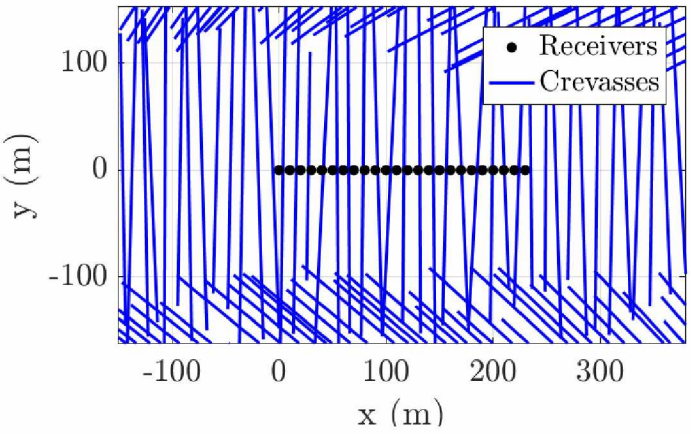

Figure 19: *GL-long* seismic line geometry. The line of receivers is parallel with the glacier axis and largely perpendicular to mid-glacier crevasses.

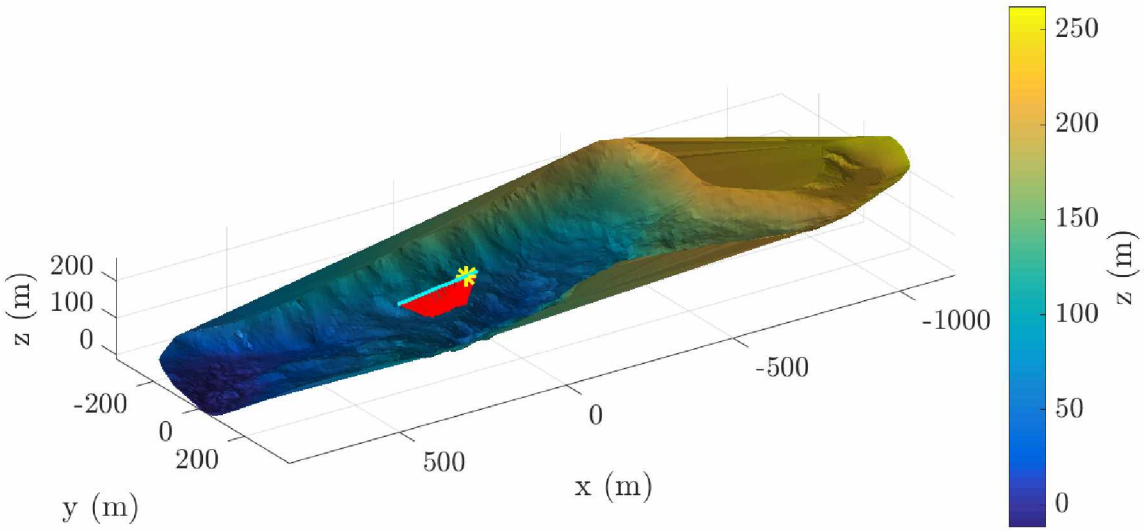

Figure 20: View of *GL-long* survey, showing raypaths from one shot. The survey samples a relatively flat area of the glacier bed.

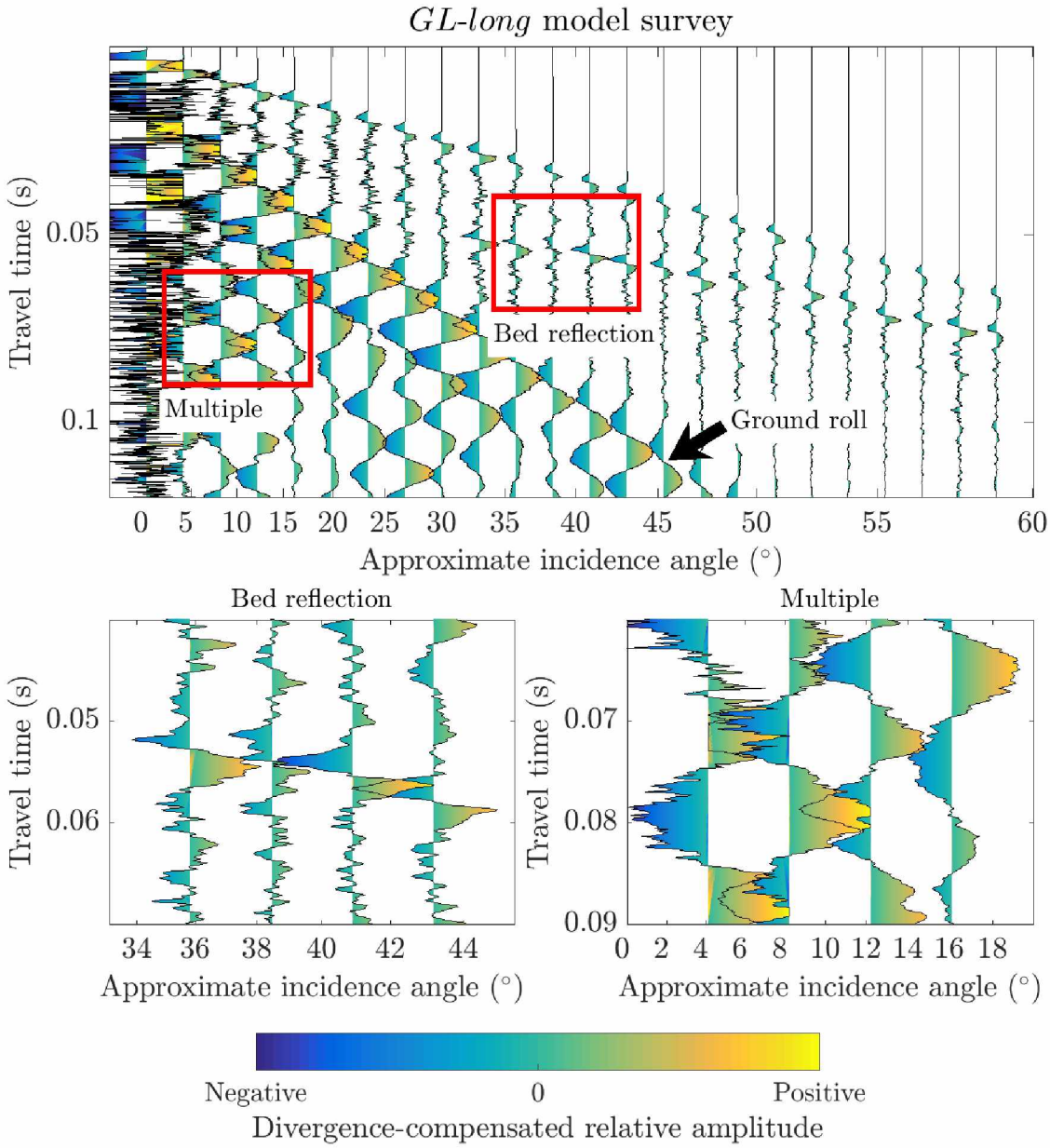

Figure 21: The section of the *GL-long* seismic record corresponding to the first shot. The bed reflection (left lower panel) is visible before the arrival of Rayleigh wave signals. Rayleigh waves overwhelm the bed reflection multiple; the multiple cannot be distinguished in the right lower panel.

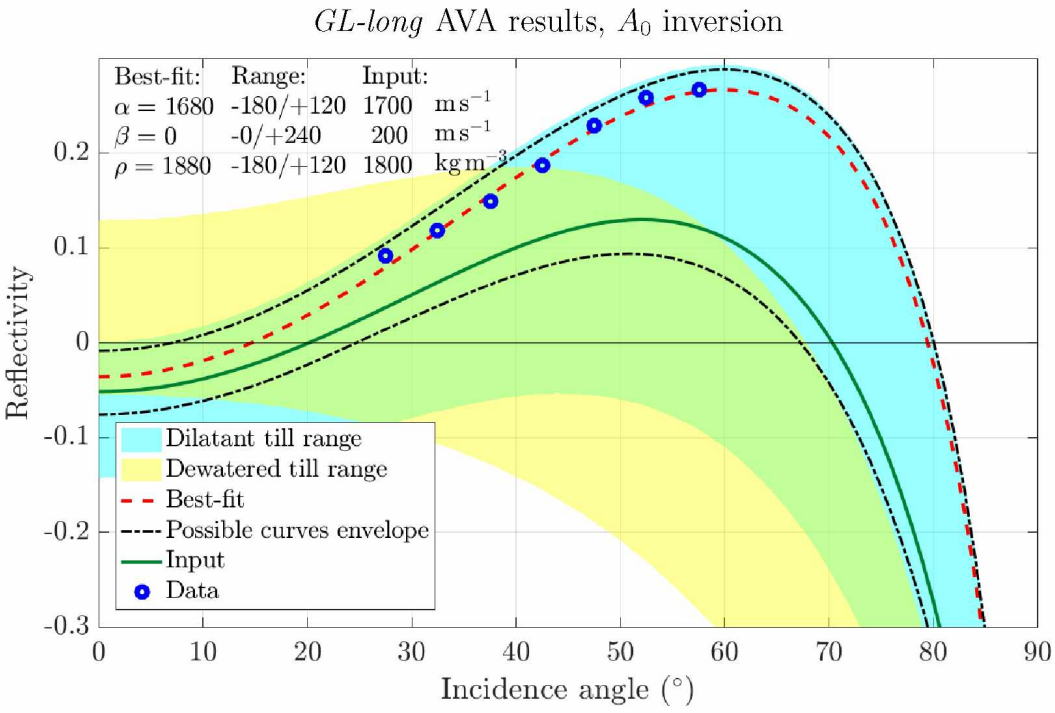

Figure 22: AVA curve fits to reflectivities calculated from the *GL-long* seismic record. Source amplitude inversion is used to calculate reflectivities.

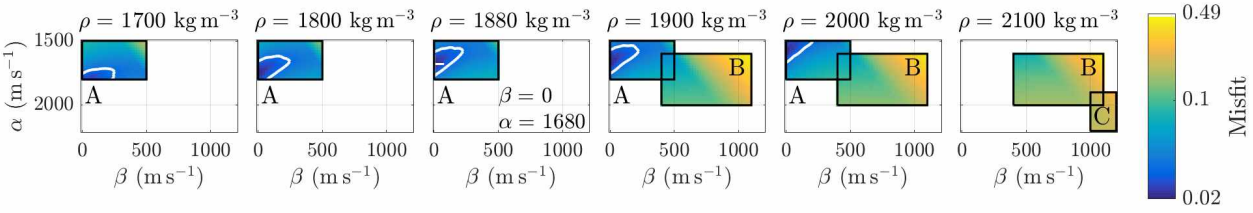

Figure 23: Misfit plots for the *GL-long* source amplitude inversion AVA curve fit.

5.3 Transverse Green Lakes Valley run ('*GL-trans*')

A geometry with a transverse seismic line (parallel to crevasses, Figure 24) produces a seismogram that looks very different from its longitudinal counterpart (Figure 26). In *GL-trans*, the bed reflection is affected by overlaying hyperbolic signals where the direct wave has reflected off of crevasses. These signals introduce confusion during the picking process, because they resemble the bed reflection (Figure 26).

Our transverse glacier cross section is more geometrically complex than our longitudinal glacier cross section. This results in irregular sampling by seismic rays, so that large segments of the geophone array sample small parts of the bed. In addition, incidence angles cannot be predicted based on offset, as demonstrated by Figure 25.

No multiple is visible at near offsets, so we must use A_0 inversion to perform AVA on this dataset. The best-fit curve indicates a dilatant till (Figure 27), though the misfit plot shows that possible parameter combinations also exist in the dewatered till range (Figure 28). Thus AVA fails to distinguish the till as dewatered or dilatant in this case.

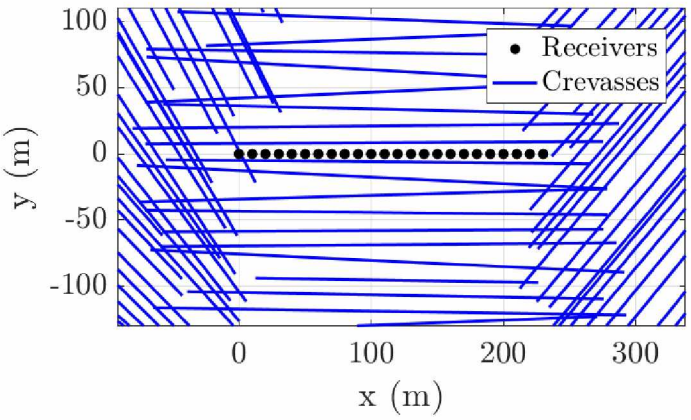

Figure 24: *GL-trans* seismic line geometry. The survey is parallel to crevasses and perpendicular to the glacier axis.

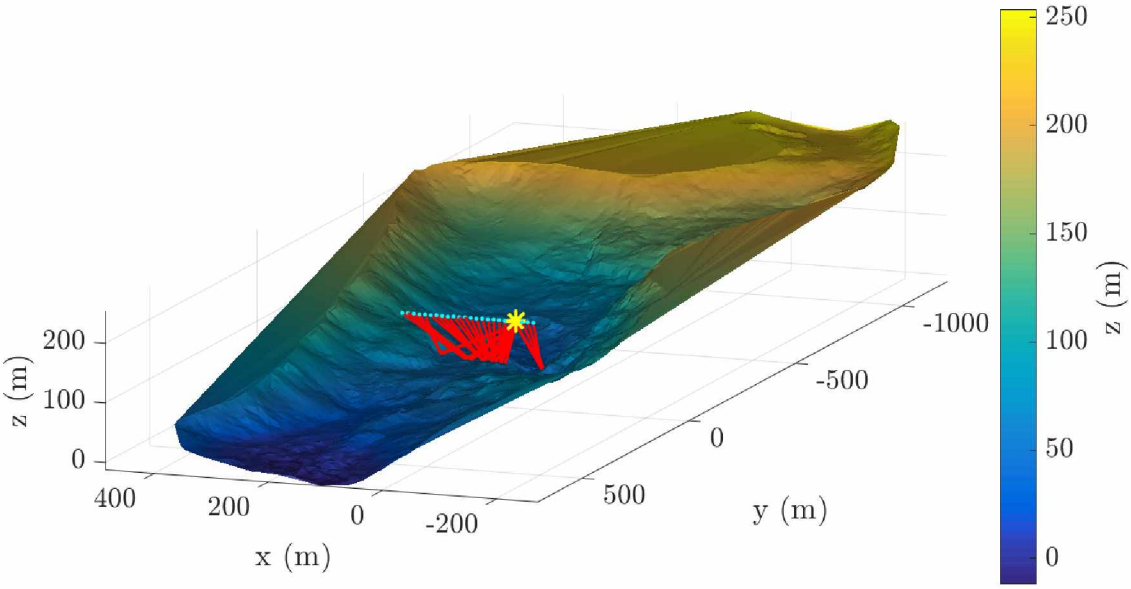

Figure 25: Greenlakes transverse survey.

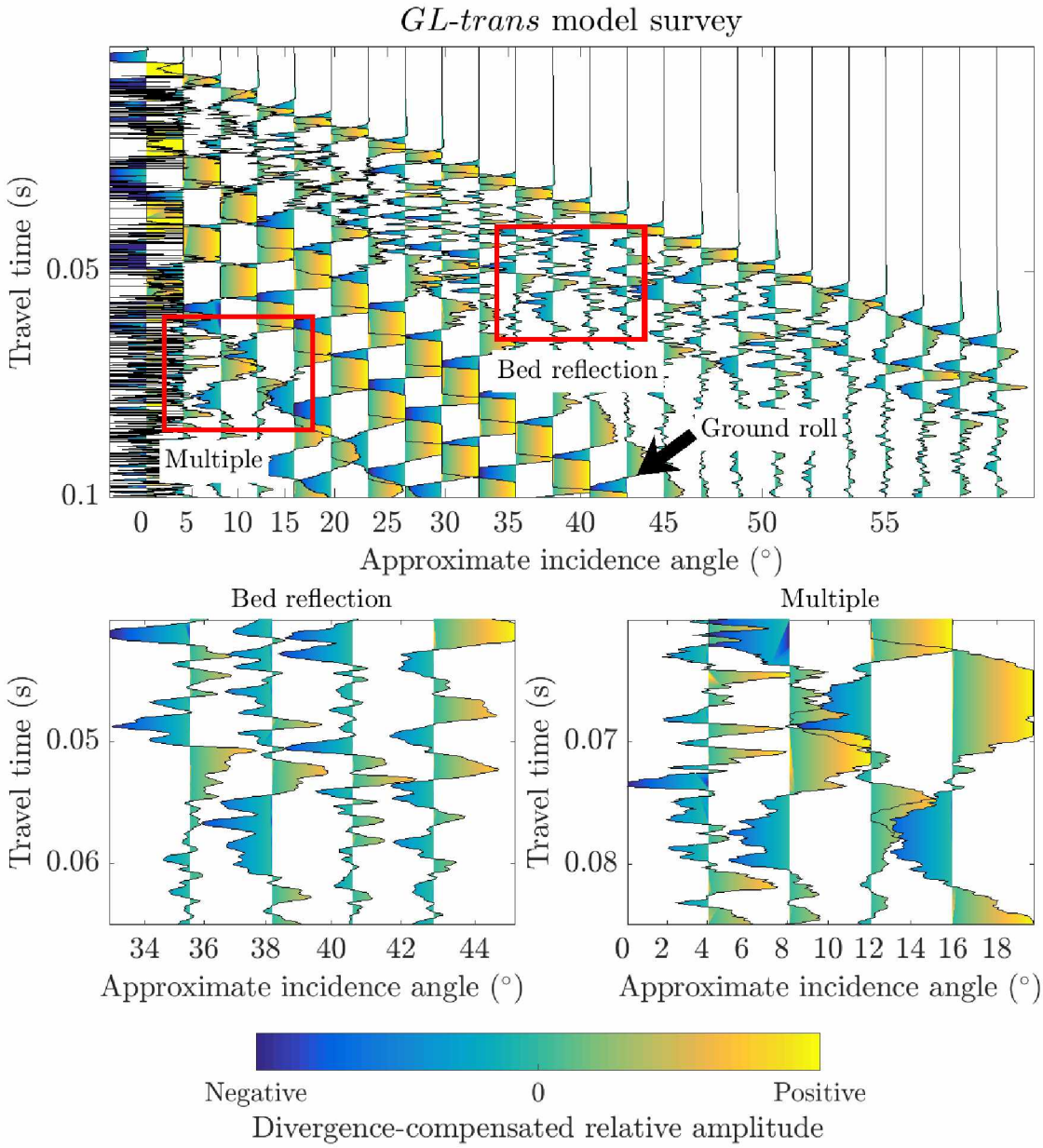

Figure 26: Traces from the first of 24 shots that comprised the *GL-trans* survey. The bed reflection is not easily distinguishable from noise, even before Rayleigh waves arrive (left lower panel). The multiple cannot be seen (right lower panel).

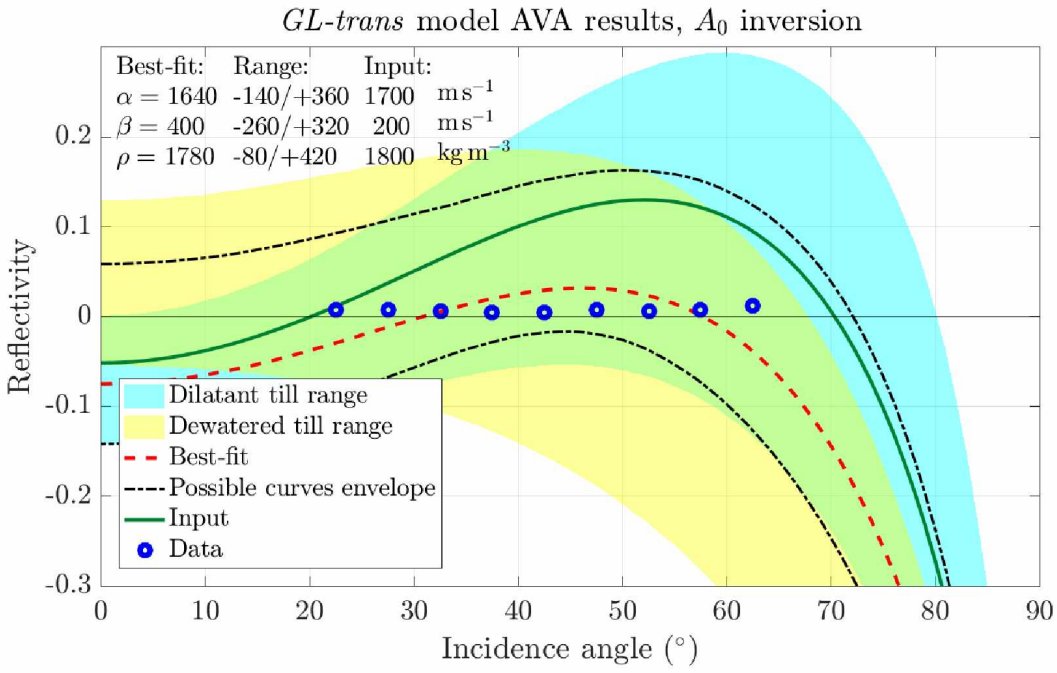

Figure 27: Source amplitude inversion AVA analysis results from the *GL-trans* survey. The envelope of acceptable curve fits encompasses large areas of both the dilatant and dewatered till ranges.

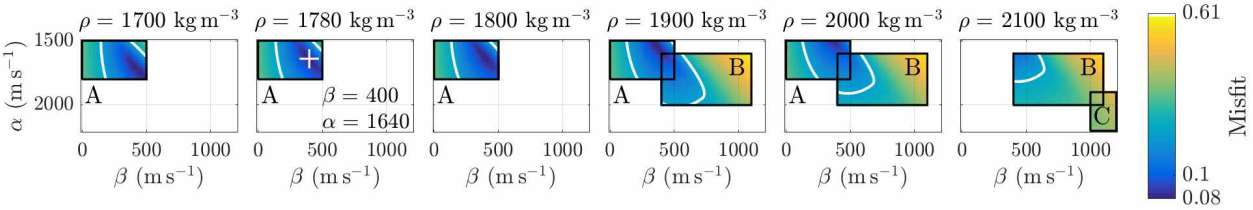

Figure 28: *GL-trans* AVA misfit plots from the source amplitude inversion AVA analysis. The best-fit value lies within the dilatant till range, though the total acceptable range spans large portions of both the dilatant and dewatered till parameter spaces.

5.4 Taku Glacier 2016 survey data analysis

The Taku Glacier seismic data did not show a clear bed reflection multiple so we perform source amplitude inversion and crossing angle analysis. Though we can see that the bed reflection is reversed in phase at near offsets, the ground roll signal obscures the zero crossing. This results in a crossing angle uncertainty of 15°. When we filter the Taku Glacier data this uncertainty drops to 5°. Crossing angle analysis of filtered data produces acceptable parameter combinations that span the dilatant till range and reach into part of the dewatered till range (Figure 29).

When we perform source amplitude inversion, our best-fit parameter combination is characteristic of a dilatant till (Figure 33), though the acceptable range still allows for the material to be a dewatered till. This is true of both raw (Figure 33, 32) and filtered data (Figures 34 and 35).

In an effort to further constrain the seismic parameters, we combine the misfit plots from the crossing angle analysis and the source amplitude inversion. All combinations of parameters that were unacceptable in the crossing angle plot are removed from the source amplitude inversion plot, and the result is shown in Figure 36. This produces the most constrained range of α, β, and ρ, but still does not eliminate parameter combinations in the dewatered range. The lowest acceptable value for shear wave velocity is $180\,\mathrm{m\,s^{-1}}$.

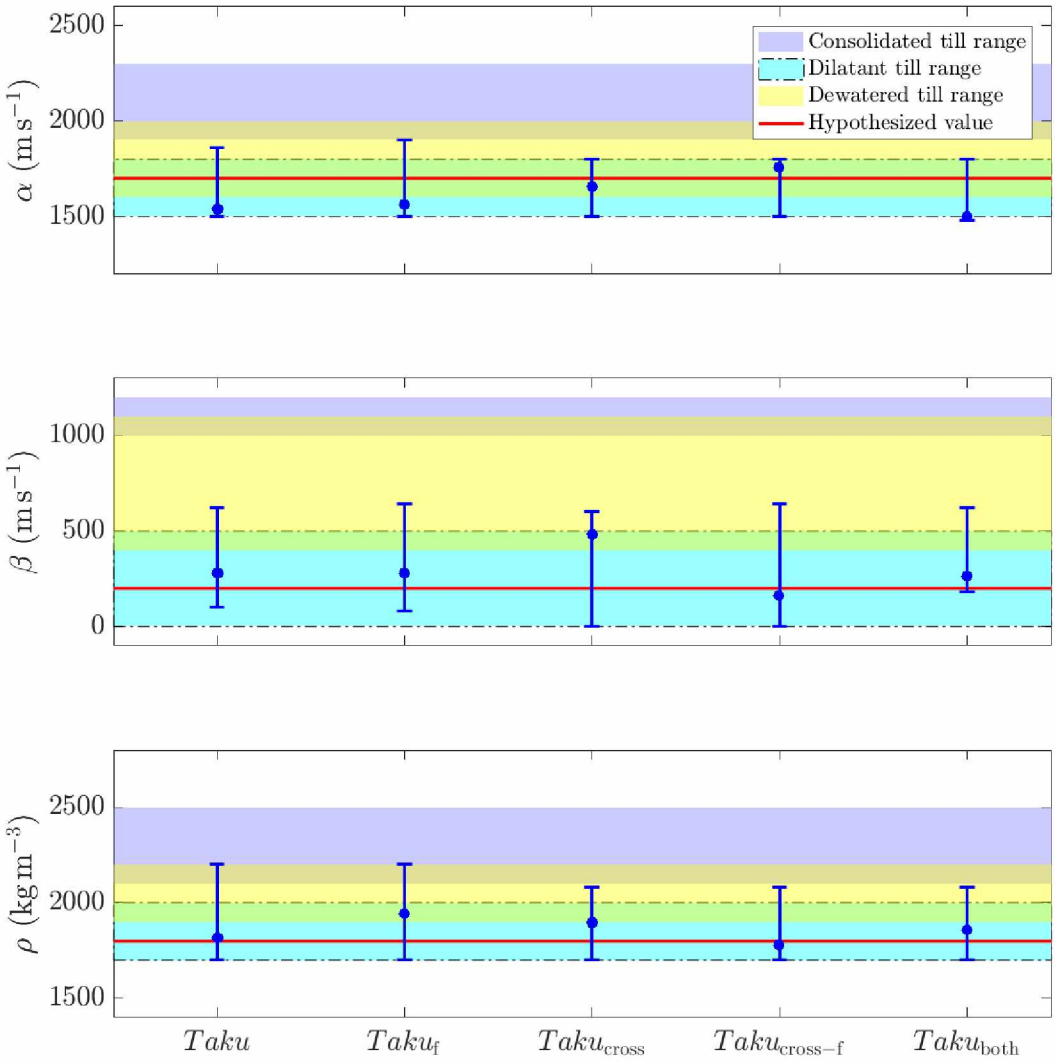

Figure 29: Parameter ranges returned by Taku Glacier AVA analysis, showing best fit values (dots) and acceptable ranges (whiskers). Chart labels refer to the following: $Taku$, the source amplitude inversion results; $Taku_{\mathrm{f}}$, source amplitude inversion of the filtered data; $Taku_{\mathrm{cross}}$, crossing angle analysis; $Taku_{\mathrm{cross-f}}$, crossing angle analysis using filtered data; and $Taku_{\mathrm{both}}$, source amplitude inversion results with all combinations not deemed acceptable by $Taku_{\mathrm{cross-f}}$ excluded.

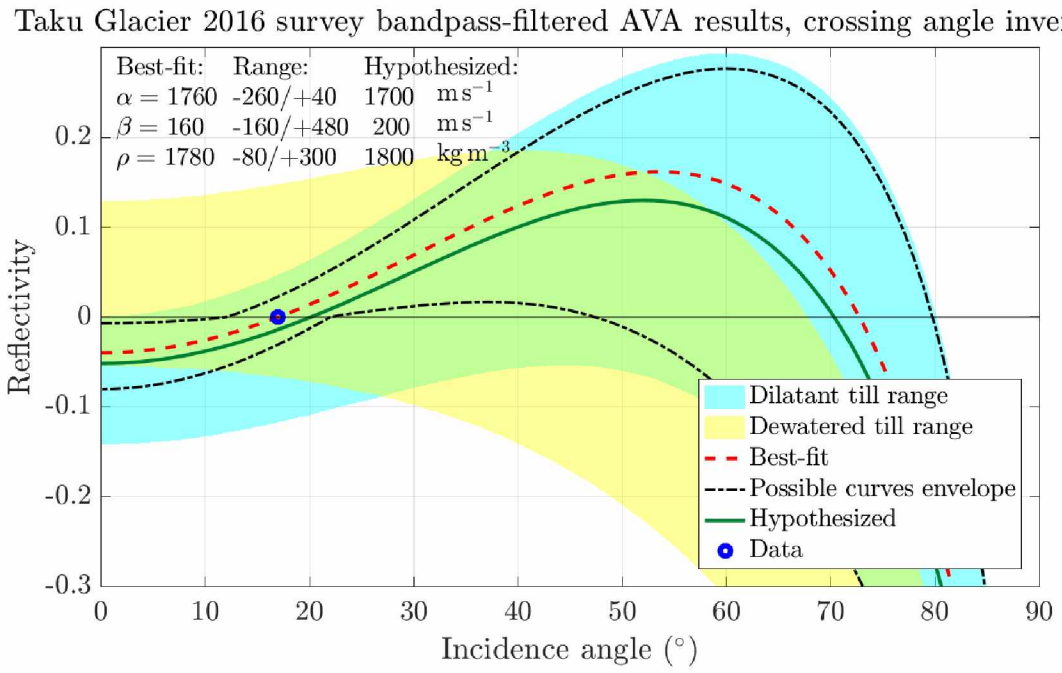

Figure 30: Crossing angle analysis results from the Taku Glacier dataset (bandpass filter applied).

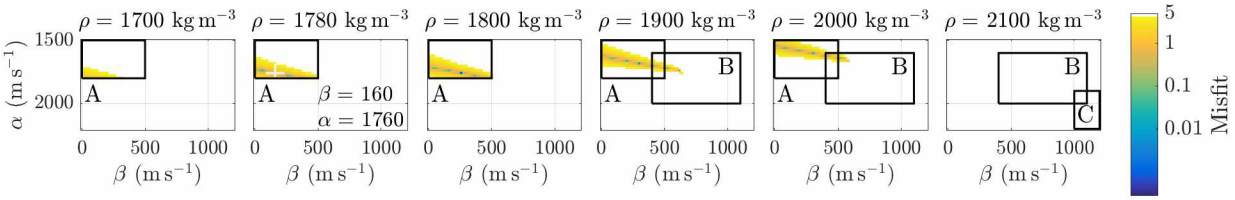

Figure 31: Taku Glacier misfit plots from crossing angle analysis of filtered data.

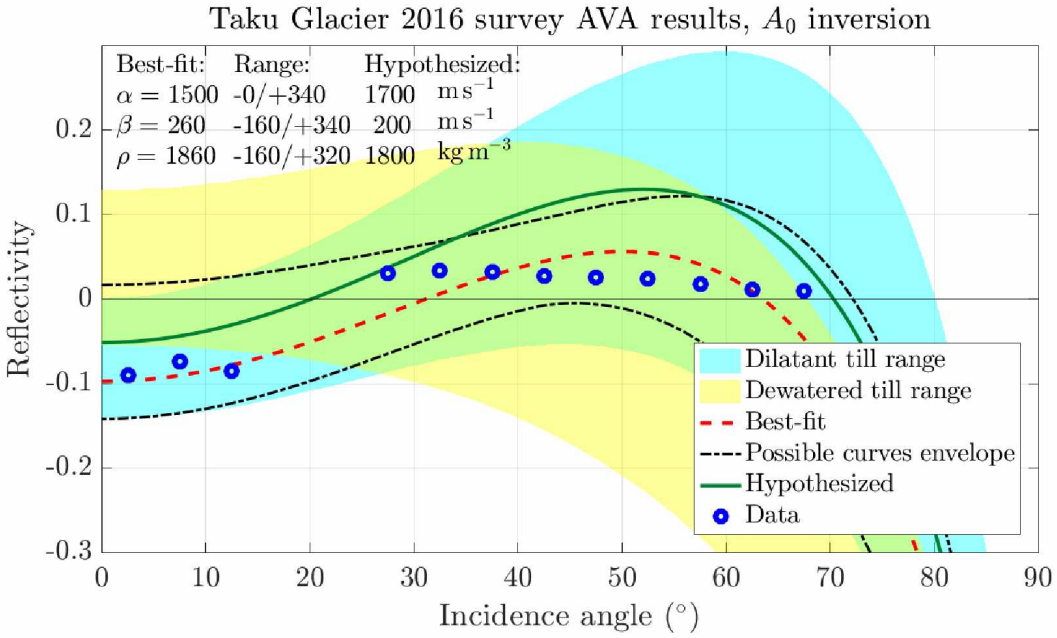

Figure 32: AVA analysis results from the Taku Glacier 2016 seismic survey. We invert for the source amplitude.

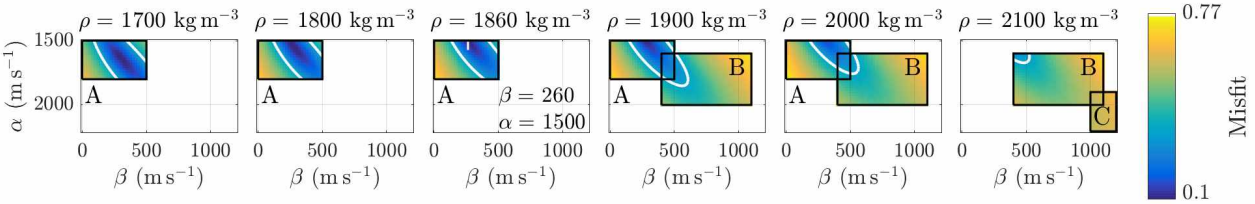

Figure 33: Taku Glacier source amplitude inversion AVA misfit.

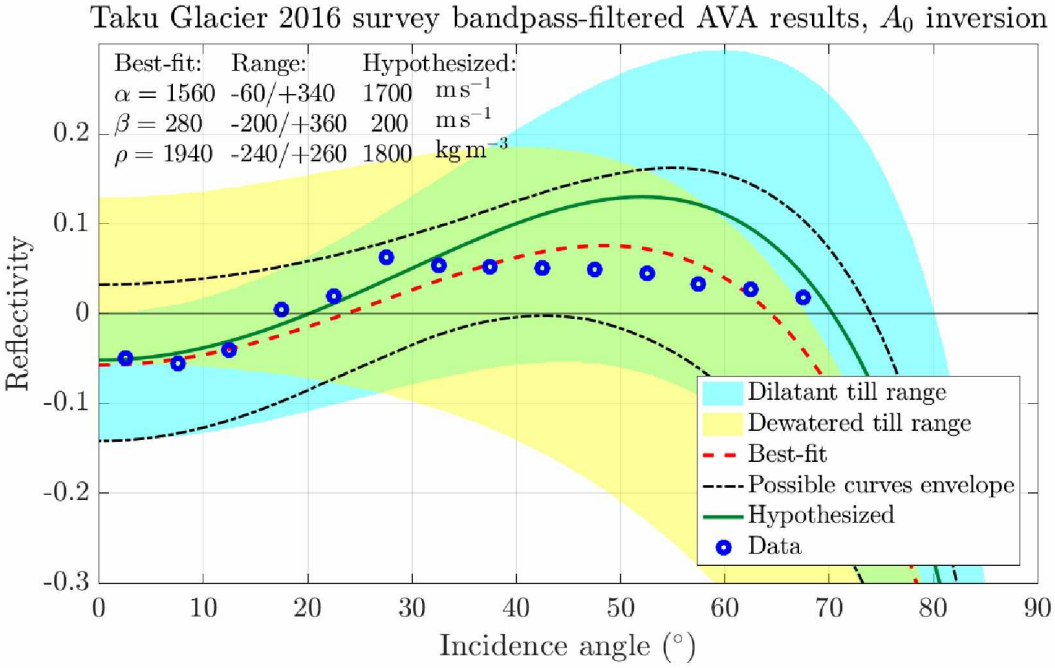

Figure 34: Source amplitude inversion results from the Taku Glacier dataset (filter applied).

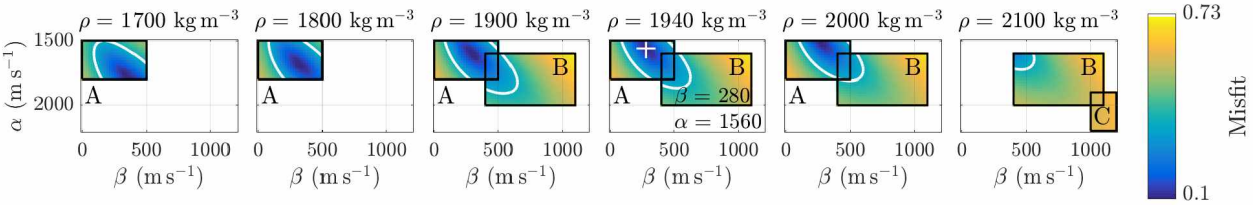

Figure 35: Taku Glacier misfit plots from the filtered source amplitude inversion.

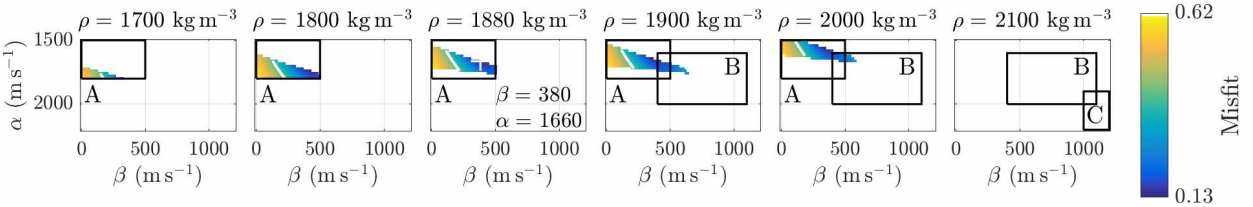

Figure 36: Combining crossing angle analysis with source amplitude inversion, Taku Glacier seismic data.

6 Discussion

6.1 Effects of crevasses

The largest impact on data quality was crevasse backscattering. We find that crevasse backscattering is strongly dependent on crevasse spacing and orientation. *GL-long* and *GL-trans* illustrate this. Though both forward models include identical crevasse geometries, *GL-long* produces a seismic record that allows AVA analysis, whereas *GL-trans* data fails AVA analysis. When our crevasses are perpendicular to the seismic line (as in *GL-long*), destructive interference results in lessened groundroll noise (Figure 37). This occurs because our crevasses are spaced at roughly 15 m intervals, which is close to one half of the starting groundroll wavelength of 28 m. Crevasses parallel to the seismic line (such as in *GL-trans*) produce signals that constructively interfere and furthermore resemble and possibly obscure the bed reflection, making picking difficult (Figure 38).

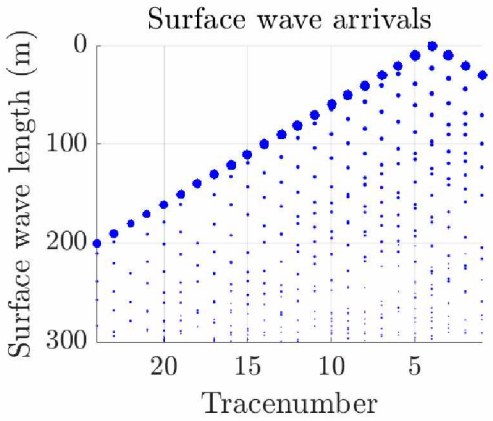

Figure 37: Crevasse raytracing results from a shot gather in the *GL-long* survey. Arrivals are plotted by ray length (a proxy for arrival time, which depends on wave type) and dot size scales with arrival amplitude. Rays reflecting off of crevasses perpendicular to the seismic line result in evenly-spaced arrivals that interfere destructively in *GL-long*.

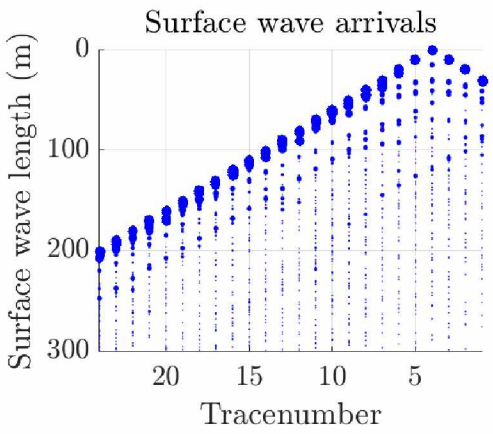

Figure 38: Crevasse raytracing results from one of the shots in the *GL-trans* survey. Reflections from crevasses parallel to the seismic line result in hyperbolic patterns in the figure which constructively interfere with one another. Consequentially the bed reflection in *GL-trans* suffers from heavy crevasse noise.

6.2 Ice thickness and AVA

At some critical thickness, the direct wave and/or its reflections off of nearby crevasses dominates the bed reflection signal even before Rayleigh waves arrive. This critical thickness is dependent on compressional wavelength, the amount and duration of noise that trails the wavelet, the spacing and orientation of crevasses, and the reflectivity of the glacier bed. In the best-case scenario (no crevasses, no noise trailing the direct wavelets) and with our model parameters, ice must be > 46 m thick to avoid interference with the bed reflection at 60° offset, or > 26 m thick if we are content with using bed reflections up to 40° offset.

This minimum thickness still allows our modeled noise trails to overlap with the reflection signals, affecting but usually not obscuring the shape of the bed reflection wavelet except at angles with very low reflectivities To avoid bed reflection contamination at 60° offset with the highest-amplitude part of our modeled noise tail, the ice thickness would need to be > 115 m. In reality this number will vary between seismic surveys depending on the length and amplitude of noise associated with the bed reflection wavelets.

Bed reflections appear clearly in *GL-trans* despite the fact that ice thickness is only 70 m, because crevasse signals interfere destructively. Without this destructive interference, the ice would have to be much thicker for the bed reflection to arrive after crevasse noise is sufficiently attenuated. Such crevasse signals seen in the Taku Glacier data last up to 0.026 s after the direct wave arrival, which brings our minimum glacier thickness up to ~ 180 m for

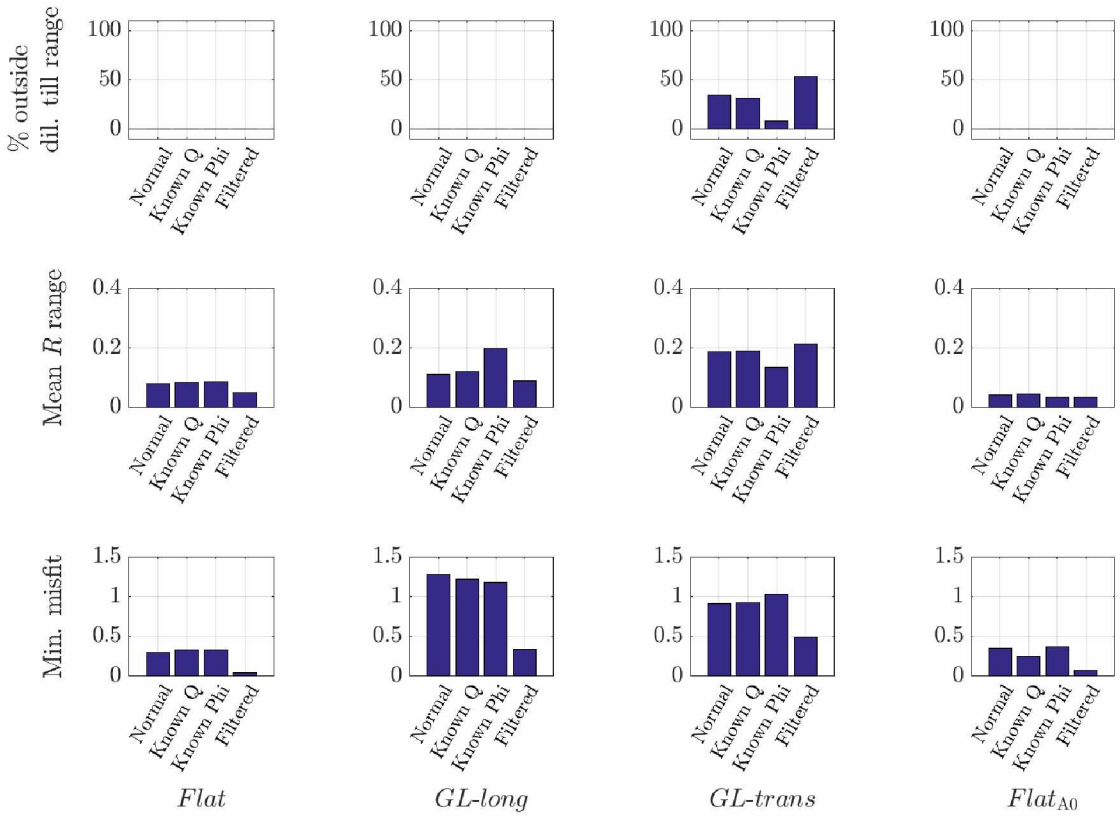

Figure 39: Metrics for accuracy and precision for synthetic model runs. Lower values indicate higher success. Top row: percent of parameter combinations that lie outside of the dilatant till range. Middle row: The mean width of the reflectivity curves envelope over the tested incidence angle range. Bottom row: the misfit between the modeled best fit and the input AVA curves over the tested range of incidence angles. Results are from source amplitude inversion analysis, except for column '$Flat_{\mathrm{A0}}$' (calculated source amplitude AVA results from the *Flat* model run). Bars in the same plot represent different improvements to the AVA analysis, either by bandpass filtering the data or substituting in the original Q or ϕ values.

60° offset. Within the bounds of 40°, this minimum thickness decreases to 100 m; in order to distinguish a reflection at incidence angles past the groundroll signal (>25°) the glacier would need to be 76 m thick. This assumes the worst case crevasse spacing for the direct compressional signal wavelength (even and continuous at increments of 22 m to 28 m). With fewer crevasses, thinner ice is acceptable.

In the case of a scenario with many crevasses parallel to the seismic line (such as *GL-trans*), surpassing the minimum thickness does not guarantee a usable bed reflection because reflection hyperbolas from crevasses could overlay the glacier bed signal at any depth.

6.3 Quality factor inversions

The only variable that influences the accuracies of our seismic quality factor calculations is the length of the seismic line. A longer seismic line results in a more accurate estimation of Q_i because deeper ice is sampled. Both *GL-long* and *GL-trans* have lines that are 230 m long. The inferred seismic quality factors are very different from the input values: Q_i is underestimated by $\sim$60 %. The *Flat* model, on the other hand, has a 1380 m long line, and calculated Q values are closer to actual values; Q_i is underestimated by $\sim$30 % (Table 5).

Underestimating Q affects the coupling correction and alters the slope of the reflectivities. The effect of overestimating attenuation is that the correction vector amplifies bed returns as receiver offset increases. To examine the importance of this effect, we re-ran AVA analysis on using the model inputs for Q_i and Q_s (Figure 39). In each plot, the first bar corresponds to the standard procedure using unfiltered data, incidence angles calculated by raytracing, and seismic quality factors calculated from the seismic line. The second bar corresponds to AVA results using the Q values from the forward model ($Q_\mathrm{i} = 170$ and $Q_\mathrm{s} = 30$). Bar charts show metrics for accuracy and precision. Accuracy is quantified by the percentage of acceptable parameter combinations that lie outside the range of a dilatant till (row 1)

Table 5: Calculated seismic quality factors from model runs.

Run name	Length (m)	Q_s	Q_i
(input)		30	170
Flat	1380	31	117
GL-long	230	41	75
GL-trans	230	10	60

and the misfit between the best-fit curve and the input curve over tested incidence angles (row 3). Row 2 quantifies precision, and shows the mean thickness of the allowable curves envelope over the tested ranges. Smaller values for all three metrics correspond to higher accuracy or precision.

Using correct Q values causes very little change in AVA results for all models using source amplitude inversion. Using known Q-values does improve the accuracy of *Flat* results when AVA is performed using the calculated source amplitude. Overall, though, results were not very sensitive to Q-value calculations, even though calculated Q-values for *GL-long* and *GL-trans* differed significantly from the prescribed values.

6.4 Reconstructions of incidence angles: the effects of incorrect ϕ

The *GL-trans* run is the most geometrically complex, and produces the least-reliable raytracing results. Depth points and incidence angles calculated using the brute stack are within a median distance of 2° and 16 m (26% of the glacier thickness) of the real forward model depth point and incidence angle values, respectively. The 75th percentile incidence angle difference is smaller than our 5° angle bins, so it seems unlikely that incidence angle miscalculations could affect our results. Figure 39 shows that AVA accuracy (measured as misfit between input and best-fit curves) does not improve with incidence angle accuracy. However, using real incidence angles does increase the percentage of the acceptable parameter combinations within the dilatant till range for *GL-trans*, which is the only model run to return a large percentage of acceptable parameter combinations outside of the dilatant till range. Interestingly, ϕ improvements resulted in decreased precision (increased envelope thickness) for *GL-long*, but increased precision for *GL-trans*. It seems that either the effects of improving ϕ are arbitrary, or incorrect ϕ assumptions improved AVA results for the wrong reason, perhaps counteracting the offset-dependent effects of noise or incorrect Q calculations.

The *GL-trans* profile overlays ice that is only 70 m deep, and yet our errors in calculated depth points range up to a few tens of meters. This would be problematic if we desired to bin bed reflections by depth point to look for spatial variability in till qualities. For *GL-trans*, we would need to choose a bin size of $\sim$30% of the ice thickness or greater to reflect this uncertainty.

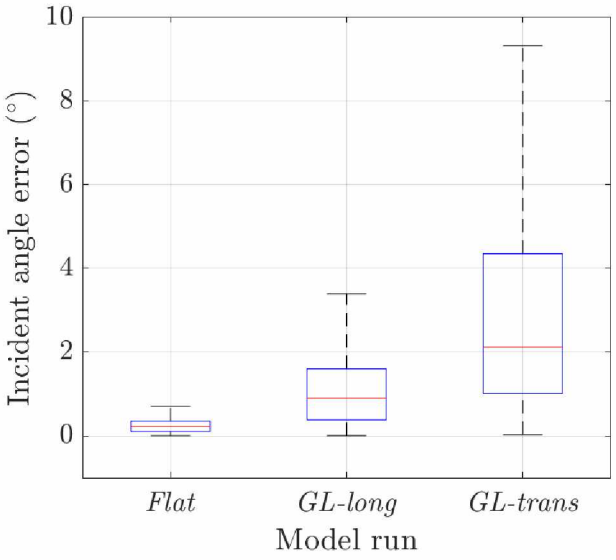

Figure 40: Box plots showing the differences between actual and calculated reflection incidence angles for all three model runs. The red lines mark the median values; blue boxes encompass the 25th and 75th percentiles; and whiskers show the full range.

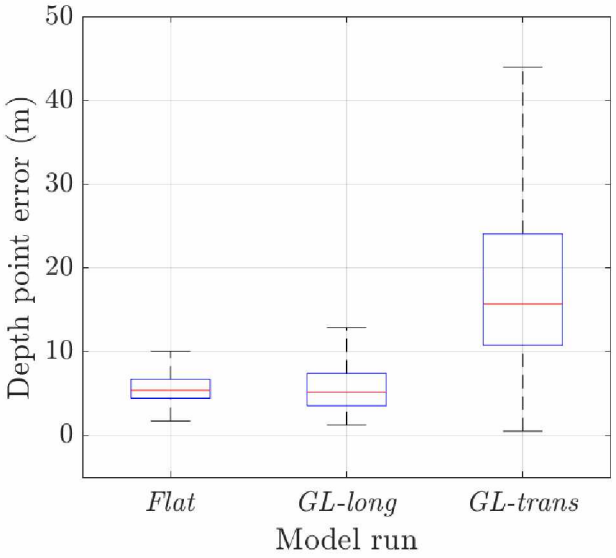

Figure 41: Box plots showing the distances between actual and calculated depth points from model runs.

6.5 Effects of filtering

Figure 39 shows that filtering generally increases the accuracy and precision of AVA analysis. With bandpass filtering, the accuracies of all model runs are improved, shown by the much lower input/best fit misfit. Filtering also narrowed the width of the curves envelope of the *Flat* and *GL-long* run.

This relationship breaks down for *GL-trans*, however. Filtering does not decrease the possible curves envelope width and does not bring results fully within the dilatant till range. It does bring the best-fit curve closer to the input curve, though this could be coincidental.

This result shows that filtering does not significantly improve the *GL-trans* AVA analysis. An important source of noise in the *GL-trans* data is the reflection of compressional waves from crevasses. The use of filtering impacts this noise as much as it does the bed reflection signal. Nevertheless, filtering *GL-trans* causes discernible peaks to appear at nearer offsets, so that we are able to fill additional incidence angle bins. However, these bins contain suspicious picks which do not bring results closer to inputs. The nearer peaks have higher amplitudes than farther-offset arrivals, which is not characteristic of the input dilatant till. Thus filtering produces artifacts that resemble bed reflections in areas that are too impacted by noise to pick before filtering.

6.6 Distinguishing till from bedrock

The *GL-trans* model run illustrates a problem with the source amplitude inversion method when no crossing angle can be observed. In order to explore the method more thoroughly, we perform a source amplitude inversion on the *GL-trans* data over a much larger range of seismic parameters and without constraints on parameter combinations. Two minima appear in the misfit plots–within the dilatant to dewatered till range, as well as in the range of bedrock parameters ($\rho = 1800\,\mathrm{kg\,m^{-3}}$ to $2400\,\mathrm{kg\,m^{-3}}$, $\alpha = 4000\,\mathrm{m\,s^{-1}}$, and $\beta = 1500\,\mathrm{m\,s^{-1}}$ to $2200\,\mathrm{m\,s^{-1}}$).

The second minimum is found because there is no obvious slope in the reflectivity versus angle curve from *GL-trans*. Dilatant tills have positive slopes over the represented range, whereas more solid materials (including bedrock) show a negative slope at far offsets. Till could be misidentified as bedrock (or vice versa) if noise obscures the slope, as it does in *GL-trans*. We did not run our forward model for a dewatered or consolidated till, but it is apparent that such firmer till types would suffer more from the limitations of the source amplitude inversion method.

One recourse to this problem is to identify the presence or absence of a critical angle in the reflectivity curve. Unlike sediments, most bedrock types experience a reflectivity spike at a specific incidence angle. This spike should be resolvable even with a large source amplitude uncertainty. However, a high geophone density is required to detect it, as the spike only spans a few degrees of incidence angle.

A second approach is to look for refracted signals late in the seismic record. Bedrock differs from sediment in that it can have a higher compressional wave velocity than glacier ice, so at far offsets critically refracted waves traveling along the bedrock will arrive at the receivers

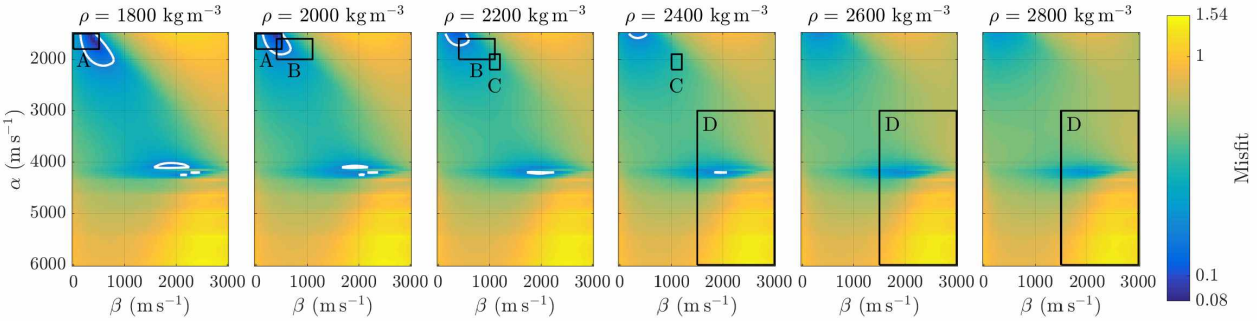

Figure 42: Misfit plots for a broad grid search, *GL-trans*. Boxes indicate parameter ranges for subglacial materials according to Table 2. A: Dilatant till range. B: Dewatered till range. C: Consolidated till range. D: Bedrock range.

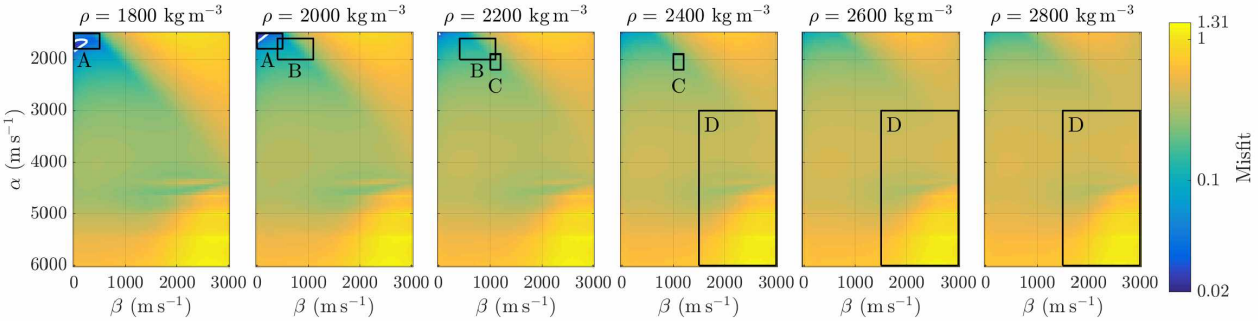

Figure 43: Misfit plots for a broad grid search, *GL-long*. Boxes indicate parameter ranges for different materials. A: Dilatant till range. B: Dewatered till range. C: Consolidated till range. D: Bedrock range. Acceptable misfit values only occur in the dilatant till range. No obvious minimum occurs elsewhere. Hence, the *GL-long* subglacial material cannot be mistaken for bedrock.

before the direct compressional wave. This appears on the record as a break in slope in the first arrivals. It is an unambiguous sign that the seismic rays are meeting bedrock.

These two solutions can fail if the rock type is of low density and low seismic velocity, such as a poorly-lithified sedimentary rock. With exceptionally poor-quality data where no reversal is visible and reflection amplitude trends are obscured, a dilatant till could be indistinguishable from poorly-lithified bedrock. A consolidated till may suffer the same effect even with reasonably reliable bed reflection amplitudes. This results in an inability to map areas of bare rock and areas of till-protected rock for glacier erosion studies. Hence thin, crevassed glaciers on poorly lithified bedrocks are difficult candidates for AVA analysis.

When source amplitude can be calculated, these problems disappear. An ice-bedrock interface is much more reflective than an ice-sediment interface at most incidence angles, resulting in stronger bed reflection and bed reflection multiple signals. Unfortunately we have demonstrated that thin crevassed glaciers have multiples obscured by groundroll noise many times the multiple amplitude, and it is unlikely that increased reflectivity will raise multiple amplitude to the point that it can be viewed in spite of ground roll.

6.7 Shot-geophone coupling corrections

We were not able to perform coupling corrections on the Taku Glacier 2016 seismic dataset because some of the direct waves were clipped, and accurate amplitudes could not be obtained from them. The results from our model runs suggest that a coupling correction is not important for Taku data analysis. Additionally, the Taku Glacier seismic dataset provided us with bed reflection amplitudes from thousands of traces. Over the course of the survey each geophone recorded returns from many different incidence angles. When we binned bed returns by incidence angle, we were stacking traces from many geophones and many shots, which should have the effect of averaging out amplitude variability.

6.8 Relationships between seismic parameters in misfit plots

Nearly all misfit plots show a positive correlation between compressional and shear wave velocities. This imparts to us the advantage that if we are able to determine the velocity of one wave type in till, we can constrain the velocity of the other wave type. This correlation is especially important in crossing angle analysis, where misfits are nearly equal everywhere along a thin diagonal line relating α and β.

One exception to this relationship is found in our *GL-long* run, where α appears to be

negatively correlated with β within our narrow grid search. When we perform a broader grid search, however, we see that the misfit plot has a complex shape (Figure 43) with a positive correlation between α and β outside of the dilatant till range.

In most misfit plots there is no correlation between ρ and β and a negative correlation between ρ and α. It is reasonable that ρ and α are negatively correlated because it is the product of the two that determines zero-incidence reflectivity. The values ρ and α are positively correlated in materials, though this relationship varies between material types and is difficult to quantify. Nevertheless this relationship could provide justification for rejecting parts of the acceptable misfit range.

7 Conclusions

This study affirms the notion that deeper, simpler, less-crevassed glaciers are the best candidates for Amplitude Variation with Angle studies (Figure 44). On the other end of the spectrum, very thin (<100 m) heavily-crevassed glaciers cannot yield data suitable for AVA analysis.

Glaciers in the middle of the spectrum–without workable bed reflection multiples, but with bed reflections that are not overwhelmed by crevasse noise–can be successful AVA candidates. Source amplitude inversion is a reasonable method that may be as accurate as regular AVA

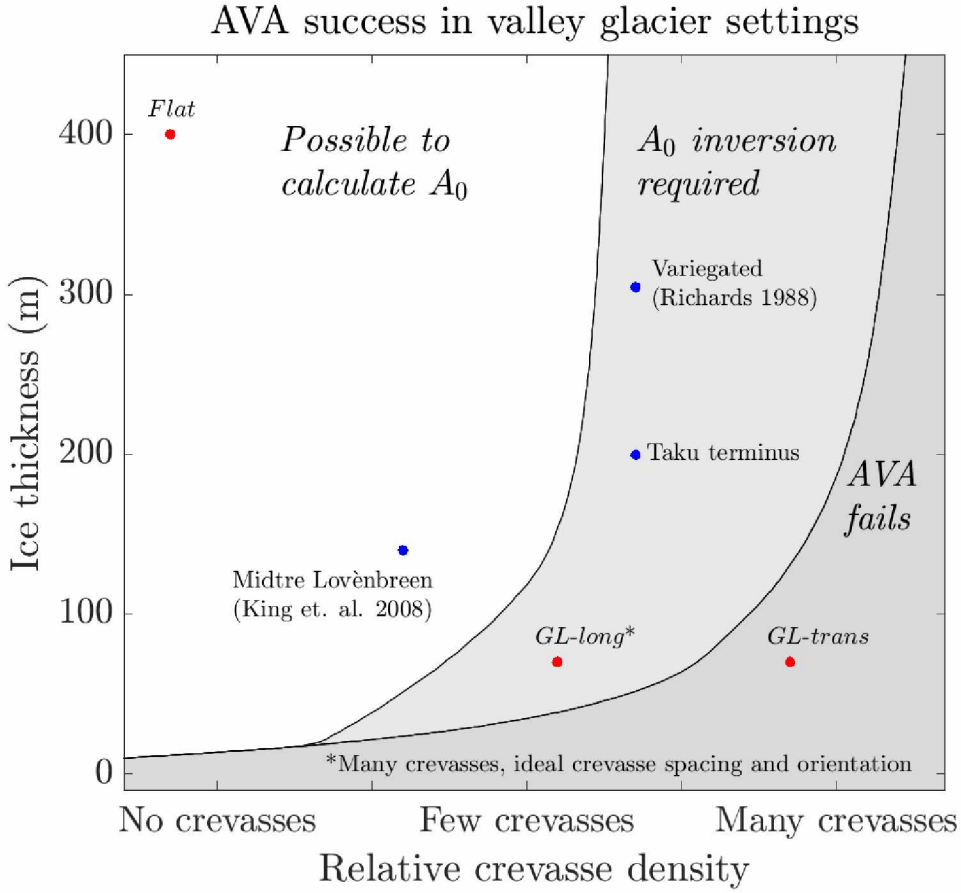

Figure 44: Conceptualization of AVA survey quality based on ice thickness and degree of crevassing. Each blue dot marks a reported reflectivity survey. Red dots are from modeled surveys. Degree of crevassing is from remarks made by the author, or we determine it from photographs or satellite imagery of the studied glacier. Though *GL-long* and *GL-trans* occur on the same model glacier, due to geometry effects *GL-long* data takes on the appearance of a less-crevassed glacier.

if the source amplitude calculation is uncertain. It avoids the possibility of unquantified errors in the source amplitude calculation skewing results. Crossing angle analysis has the potential to add additional constraints and if possible should be performed in addition to source amplitude inversion.

We also suggest forgoing source-receiver coupling corrections, unless coupling variability is large, the number of shots and geophones is limited, or improvements are made on our method of calculating Q. Source-receiver coupling corrections are hampered by miscalculations of seismic quality factor, which could lead to errors that exceed the coupling variability. Such errors introduce a systematic error to AVA analysis, while coupling variability is more likely to average out within angle bins in a multi-shot survey.

This forward model serves as a planning tool for seismic surveys on thin, crevassed, geometrically-complex glaciers. Crevasse locations can be obtained from satellite imagery of the glacier surface. The glacier bed can be constrained using existing radar data or, barring that, an estimated glacier bed that combines a typical glacier width/depth ratio with the maximum amount of basal topography that can be reasonably expected. If AVA is successful from the simulated data despite the high amplitude of basal topography, then it should be successful with the study glacier. The model could be run with the hypothesized till parameters and perhaps repeated with the the local bedrock to ensure the two can be distinguishable from each other. Model results can also indicate the best use of resources in the seismic survey. If the bed reflection is obscured at near offsets due to crevasse noise, researchers can plan to locate shots farther away from the geophone line. However, this will make it impossible to use a direct calculation of the source amplitude.

Our synthetic survey results show that geometry uncertainties and Q uncertainties do not significantly impact AVA results. Because of this, we are confident that the Taku Glacier AVA results are not misleading, even without coupling corrections and with only an estimate of the glacier bed shape. Our brute stack did not show a basal topography that was as severe as the *GL-trans* topography, so our ϕ calculation errors could not have exceeded the *GL-trans* errors. It is probable that the Taku Glacier incidence angle calculation errors were smaller than the size of our angle bins, so the topography beneath the Taku Glacier seismic line could not have caused a till type misidentification.

Source amplitude inversion and crossing angle analysis suggest but do not guarantee that Taku Glacier sediments are within the range we have defined as dilatant. When we combine crossing angle analysis with source amplitude inversion, our best-fit seismic parameters are $\alpha = 1660\,\mathrm{m\,s^{-1}}$, $\beta = 380\,\mathrm{m\,s^{-1}}$, and $\rho = 1880\,\mathrm{kg\,m^{-3}}$, indicative of a dilatant till. However,

allowable values for ρ and β exceed the dilatant till range. The highest possible value for ρ is $2080\,\mathrm{kg\,m^{-3}}$, and β can range up to $640\,\mathrm{m\,s^{-1}}$. This maximum density corresponds to a porosity of 33 %. Based on these results we can conclude that the till is either deformable or is soft enough to reach a deformable state under the right conditions.

A deformable till under Taku Glacier has consequences for its terminus evolution. Till deformation allows faster evacuation of sediments from beneath Taku Glacier, as deforming till creeps towards subglacial channels.

Acknowledgements

The forward model described in this thesis was developed by Adam Booth (of Imperial College London at the time, currently at University of Leeds) and myself. I continued to modify the model afterwards, and performed all of the model runs and analysis of model results. I also performed the analysis of the Taku Glacier 2016 seismic data and led the 2016 seismic survey.

The Taku 2016 survey was made possible by input and assistance from Martin Truffer and help from Thomas Hart (blaster), Aurora Roth, and Andy Aschwanden. Special thanks to Alessio Gusmeroli, who designed the first Taku Glacier seismic survey and taught me how to acquire and process seismic data. IRIS PASSCAL (The Incorporated Research Institutions for Seismology Portable Array Seismic Studies of the Continental Lithosphere Instrument Center) provided seismic recording equipment for the Taku 2016 seismic survey. Thanks to Peter Burkett, Sridhar Anandakrishnan, and Kiya Riverman for instrument support, and to Bernard Hallet and Esther Babcock for their input and advice. This project is funded by National Science Foundation grant number 1304899, and by the University of Alaska Fairbanks Center for Global Change Student Research Grant with funds from the Cooperative Institute for Alaska Research.

References

Aki, K., and P. G. Richards (2002), *Quantitative Seismology*, second ed., University Science Books, San Francisco.

Aldridge, G. F. (1990), Short note: the Berlage wavelet, *Geophysics*, *55*(11), 1508–1511.

Alley, R. B. (1991), Sedimentary processes may cause fluctuations of tidewater glaciers, *Annals of Glaciology*, *15*, 119–124.

Alley, R. B., D. D. Blankenship, and C. R. Bentley (1987), Till beneath Ice Stream B: 3. Till deformation: evidence and implications, *Journal of Geophysical Research*, *92*(B9), 8921–8929.

Anandakrishnan, S. (2003), Dilatant till layer near the onset of streaming flow of Ice Stream C, West Antarctica, determined by AVO (amplitude vs offset) analysis, *Annals of Glaciology*, *36*, 283–286, doi:10.3189/172756403781816329.

Anandakrishnan, S., D. D. Blankenship, R. B. Alley, and P. L. Stoffa (1998), Influence of subglacial geology on the position of a West Antarctic ice steam from seismic observations, *Nature*, *394*(September), 62–65, doi:10.1038/nature01200.1.

Anderson, R. S. (2014), Evolution of lumpy glacial landscapes, *Geology*, (August), 679–682, doi:10.1130/G35537.1.

Babcock, E., and J. Bradford (2014), Quantifying the basal conditions of a mountain glacier using a targeted full-waveform inversion: Bench Glacier, Alaska, USA, *Journal of Glaciology*, *60*(224), 1221–1231, doi:10.3189/2014JoG14J072.

Benjumea, B., and T. Teixidó (2001), Seismic reflection constraints on the glacial dynamics of Johnsons Glacier, Antarctica, *Journal of Applied Geophysics*, *46*(1), 31–44, doi:10.1016/S0926-9851(00)00037-9.

Blankenship, D. D., C. R. Bentley, S. T. Rooney, and R. B. Alley (1986), Seismic measurements reveal a saturated porous layer beneath an active Antarctic ice stream, *Nature*, *322*(6074), 54–57, doi:10.1038/322054a0.

Blankenship, D. D., C. R. Bentley, S. T. Rooney, and R. B. Alley (1987), Till beneath ice stream B: 1. Properties derived from seismic travel times, *Journal of Geophysical Research*, *92*(B9), 8903, doi:10.1029/JB092iB09p08903.

Booth, A. D., R. A. Clark, B. Kulessa, T. Murray, J. Carter, S. Doyle, and A. Hubbard (2012), Thin-layer effects in glaciological seismic amplitude-versus-angle (AVA) analysis: Implications for characterising a subglacial till unit, Russell Glacier, West Greenland, *Cryosphere*, *6*, 909–922, doi:10.5194/tc-6-909-2012.

Booth, A. D., E. Emir, and A. Diez (2016), Approximations to seismic AVA responses : Validity and potential in glaciological applications, *Geophysics*, *81*(1), WA1–WA11, doi: 10.1190/geo2015-0187.1.

Boulton, G. S., and D. L. Dent (1974), The nature and rates of post-depositional changes in recently deposited till from south-east Iceland, *Geografiska Annaler*, *56A*(3), 121–134.

Castagna, J. P., H. W. Swan, and D. J. Foster (1998), Framework for AVO gradient and intercept interpretation, *Geophysics*, *63*(3), 948, doi:10.1190/1.1444406.

Christianson, K., L. E. Peters, R. B. Alley, S. Anandakrishnan, R. W. Jacobel, K. L. Riverman, A. Muto, and B. A. Keisling (2014), Dilatant till facilitates ice-stream flow in northeast Greenland, *Earth and Planetary Science Letters*, *401*, 57–69, doi: 10.1016/j.epsl.2014.05.060.

Clark, C. D. (2010), Emergent drumlins and their clones: from till dilatancy to flow instabilities, *51*(200), 1011–1025.

Clarke, B. G., D. B. Hughes, and S. Hashemi (2008), Physical characteristics of subglacial tills, *Geotechnique*, *58*(1), 67–76, doi:10.1680/geot.2008.58.1.67.

Clee, T. E., J. C. Savage, and K. G. Neave (1969), Internal Friction in Ice near Its Melting Point, *Journal Geophysical Research*, *74*(4), 973–980.

Cuffey, K. M., and R. B. Alley (1996), Is erosion by deforming subglacial sediments significant? (Toward till continuity), *Annals of Glaciology*, *22*, 17–24.

Dow, C., A. Hubbard, A. Booth, S. Doyle, A. Gusmeroli, and Y. B. Kulessa (2013), Seismic evidence of mechanically weak sediments underlying Russell Glacier, West Greenland, *Annals of Glaciology*, *54*(64), 135–141, doi:10.3189/2013AoG64A032.

Gehrels, G. E., and H. C. Berg (1992), Geologic map of Southeastern Alaska, *U.S Geological Survey map I-1867*.

Gusmeroli, A., R. A. Clark, T. Murray, A. D. Booth, B. Kulessa, and B. E. Barrett (2010), Instruments and Methods: Seismic wave attenuation in the uppermost glacier ice of Storglaciären, Sweden, *Journal of Glaciology*, *56*(196), 249–256.

Hamilton, E. L. (1976), Shear-wave velocity versus depth in marine sediments: a review, *Geophysics*, *41*(5), 985–996.

Hart, J. K., K. C. Rose, and K. Martinez (2011), Subglacial till behaviour derived from in situ wireless multi-sensor subglacial probes: Rheology, hydro-mechanical interactions and till formation, *Quaternary Science Reviews*, *30*(1-2), 234–247, doi: 10.1016/j.quascirev.2010.11.001.

Hewitt, I. J. (2011), Modelling distributed and channelized subglacial drainage: the spacing of channels, *Journal of Glaciology*, *57*(202), 302–314, doi:10.3189/002214311796405951.

Iverson, N., T. S. Hooyer, and R. W. Baker (1998), Ring-shear studies of till deformation: Coulomb-plastic behaviour and distributed strain in glacier beds, *Journal of Glaciology*, *44*, 634–642.

Iverson, N. R. (2010), Shear resistance and continuity of subglacial till: Hydrology rules, *Journal Of Glaciology*, *56*(200), 1104–1114.

Iverson, N. R., P. Jansson, and R. L. Hooke (1994), In-situ measurement of the strength of deforming subglacial till, *Journal of Glaciology*, *40*(136), 497–503.

Iverson, N. R., B. Hanson, R. L. Hooke, and P. Jansson (1995), Flow mechanism of glaciers on soft beds., *Science*, *267*(5194), 80–81, doi:10.1126/science.267.5194.80.

Kamb, B. (1991), Rheological nonlinearity and flow instability in the deforming bed mechanism of ice stream motion, *Journal of Geophysical Research*, *96*(B10), 16,585, doi: 10.1029/91JB00946.

King, E. C., A. M. Smith, T. Murray, and G. W. Stuart (2008), Glacier-bed characteristics of midtre Lovénbreen, Svalbard, from high-resolution seismic and radar surveying, *Journal of Glaciology*, *54*(184), 145–156, doi:10.3189/002214308784409099.

Kjartansson, E. (1979), Constant Q-wave propagation and attenuation, *Journal Geophysical Research*, *84*, 4737–4748.

Krebes, E., and G. F. Margrave (1991), Zoeppritz [Computer software], *CREWES Toolbox Version 1272, syntraces*, https://www.crewes.org/ResearchLinks/FreeSoftware/.

Luthra, T., S. Anandakrishnan, J. P. Winberry, R. B. Alley, and N. Holschuh (2016), Basal characteristics of the main sticky spot on the ice plain of Whillans Ice Stream, Antarctica, *Earth and Planetary Science Letters*, *440*, 12–19, doi:10.1016/j.epsl.2016.01.035.

Margrave, G. F. (1999), Einar [Computer software], *CREWES Toolbox Version 1272, Qtools*, https://www.crewes.org/ResearchLinks/FreeSoftware/.

Medwin, H. (1975), Speed of Sound In Water: A Simple Equation for Realistic Parameters, *The Journal of the Acoustical Society of America*, *58*(6), 1318–1319.

Morgan, N. A. (1969), Physical properties of marine sediments as related to seismic velocities, *Geophysics*, *34*(4), 529–545.

Motyka, R. J., and J. E. Begét (1996), Taku Glacier, southeast Alaska, U.S.A.: Late Holocene history of a tidewater glacier, *Arctic and Alpine Research*, *28*, 42–51, doi:10.2307/1552084.

Motyka, R. J., M. Truffer, E. M. Kuriger, and A. K. Bucki (2006), Rapid erosion of soft sediments by tidewater glacier advance: Taku Glacier, Alaska, USA, *Geophysical Research Letters*, *33*(24), 1–5, doi:10.1029/2006GL028467.

Navarro, F. J., Y. Y. Macheret, and B. Benjumea (2005), Application of radar and seismic methods for the investigation of temperate glaciers, *Journal of Applied Geophysics*, *57*, 193–211, doi:10.1016/j.jappgeo.2004.11.002.

Nolan, M., R. J. Motkya, K. Echelmeyer, and D. C. Trabant (1995), Ice-thickness measurements of Taku Glacier, Alaska, USA, and their relevance to its recent behavior.

O'Neel, S. O., K. A. Echelmeyer, and R. J. Motyka (2003), Short-term variations in calving of a tidewater glacier : LeConte Glacier, Alaska, U.S.A., *Journal of Glaciology*, *49*(167), 587–598.

Peters, L. E. (2009), A seismic investigation of basal conditions in glaciated regions, Ph.D. thesis, Pennsylvania State University.

Peters, L. E., S. Anandakrishnan, R. B. Alley, J. P. Winberry, D. E. Voigt, A. M. Smith, and D. L. Morse (2006), Subglacial sediments as a control on the onset and location of two

Siple Coast ice streams, West Antarctica, *Journal of Geophysical Research: Solid Earth*, *111*, 1–14, doi:10.1029/2005JB003766.

Peters, L. E., S. Anandakrishnan, R. B. Alley, and A. M. Smith (2007), Extensive storage of basal meltwater in the onset region of a major West Antarctic ice stream, *Geology*, *35*, 251–254, doi:10.1130/G23222A.1.

Peters, L. E., S. Anandakrishnan, C. W. Holland, H. J. Horgan, D. D. Blankenship, and D. E. Voigt (2008), Seismic detection of a subglacial lake near the South Pole, Antarctica, *Geophysical Research Letters*, *35*(L23501), doi:10.1029/2008GL035704.

Pfeffer, W. T., J. Cohn, M. Meier, and R. M. Krimmel (2000), Alaskan Glacier beats a dramatic retreat, *Eos Trans. AGU*, *81*(48), 577, doi:10.1029/EO081i048p00577.

Post, A. (1975), Preliminary hydrology and historic terminal changes of Columbia Glacier, Alaska, *U.S. Geolological Survey Hydrologic Investigations Atlas*, (map HA-559).

Post, A., and R. J. Motyka (1995), Taku and LeConte Glaciers, Alaska: Calving-Speed of Late-Holocene Asynchronous advances and Retreats, *Physical Geography*, *16*, 59–82.

Rathbun, A. P., C. Marone, R. B. Alley, and S. Anandakrishnan (2008), Laboratory study of the frictional rheology of sheared till, *Journal of Geophysical Research*, *113*(F2), 1–14, doi:10.1029/2007JF000815.

Reinardy, B. T. I., R. D. Larter, C. D. Hillenbrand, T. Murray, J. F. Hiemstra, and A. D. Booth (2011), Streaming flow of an Antarctic Peninsula palaeo-ice stream, both by basal sliding and deformation of substrate, *Journal of Glaciology*, *57*(204), 596–608, doi:10.3189/002214311797409758.

Richards, M. A. (1988), Seismic evidence for a weak basal layer during the 1982 surge of Variegated Glacier, Alaska, USA, *Journal of Glaciology*, *34*(116), 111–120.

Sheriff, R. E., and L. P. Geldart (1995), *Exploration Seismology*, second ed., Cambridge University Press, New York.

Talalay, P. G. (2013), Subglacial till and bedrock drilling, *Cold Regions Science and Technology*, *86*, 142–166, doi:10.1016/j.coldregions.2012.08.009.

Truffer, M., and W. D. Harrison (2006), In situ measurements of till deformation and water pressure, *Journal of Glaciology*, *52*(177), 175–182, doi:10.3189/172756506781828700.

Truffer, M., W. Harrison, and K. A. Echelmeyer (2000), Glacier motion dominated by processes deep in underlying till, *Journal of Glaciology*, *46*(153), 213–221, doi: 10.3189/172756500781832909.

Truffer, M., K. A. Echelmeyer, and W. D. Harrison (2001), Implications of till deformation on glacier dynamics, *Journal of Glaciology*, *47*(156), 123–134, doi: 10.3189/172756501781832449.

Truffer, M., R. J. Motyka, M. Hekkers, I. M. Howat, and M. King (2009), Terminus dynamics at an advancing glacier: Taku Glacier, Alaska, *Journal of Glaciology*, *55*(194), 1052–1060, doi:10.3189/002214309790794887.

Tulaczyk, S. (1999), Ice sliding over weak, fine-grained tills: Dependence of ice-till interactions on till granulometry, *Geological Society of America Special Papers*, *337*, 159–177, doi:10.1130/0-8137-2337-X.159.

Vaughan, D. G., A. M. Smith, P. C. Nath, and E. Le Meur (2003), Acoustic impedence and basal shear stress beneath four Antarctic ice streams, *Annals of Glaciology*, *36*, 225–232, doi:10.3189/172756403781816437.

Walder, J. S., and A. C. Fowler (1994), Channelized subglacial drainage over a deformable bed, *Journal of Glaciology*, *40*(134), 3–15.

Walter, F., J. Chaput, and M. P. Lüthi (2014), Thick sediments beneath Greenland's ablation zone and their potential role in future ice sheet dynamics, *Geology*, *42*(6), 487–490, doi: 10.1130/G35492.1.

Widess, M. B. (1973), How thin is a thin bed?, *Geophysics*, *38*(6), 1176–1180.

Zoeppritz, K. (1919), VII b. Über Reflexion und Durchgang seismischer Wellen durch Unstetigkeitsflächen, *Nachrichten von der Gesellschaft der Wissenschaften zu Göttingen, Mathematisch-Physikalische Klasse*, *1919*, 66–84.